Capillary Coatings: Flow and Drying Dynamics in Open Microchannels

Robert K. Lade Jr., Krystopher S. Jochem, Christopher W. Macosko, and Lorraine F. Francis*

Department of Chemical Engineering and Materials Science, University of Minnesota – Twin Cities, 421 Washington Ave. SE, Minneapolis MN, 55455, United States

Abstract

Capillary flow and drying of polymer solutions in open microchannels are explored over timescales spanning seven orders of magnitude, from capillary filling $(10^{-3}-10 \text{ s})$ to the formation of a dry thin film (a 'capillary coating': 10^2-10^3 s). During capillary filling, drying-induced changes (increased solids content and viscosity) generate micro-scale pinning events that impede contact line motion. Three unique types of pinning are identified and characterized, each defined by the specific location(s) along the contact line at which pinning is induced. Drying is shown to ultimately pin the contact line permanently and the associated total flow distances and times are revealed to be strong functions of channel width and drying rate. In general, lower drying rates coupled with intermediate channel widths are found to be most conducive to longer flow distances and times. After the advancing contact line permanently pins, internal flows driven by uneven evaporation rates continue to drive polymer to the contact line. This phenomenon promotes a local accumulation of solids and persists until all motion is arrested by drying. The effect of channel width and drying rate are investigated at each stage of this capillary coating process. These results are then applied to case studies of two functional inks commonly used in printed electronics fabrication: a PEDOT (poly(3,4ethylenedioxythiophene)) and a graphene ink. While drying is shown to permanently arrest flow in both inks, both systems exhibit an increased resistance to pinning unexplained by mechanisms identified in aqueous polymer systems. Instead, arguments based on chemistry, particle size, and rheology are used to explain their novel behavior. These case studies provide insight into how functional inks can be better designed to optimize flow distances and maximize overall dry film uniformity in capillary coatings.

Introduction

Capillarity is an effective and universal driving force. In microchannels—micron-scale conduits for capillary flow—capillarity provides a convenient and precise means of handling and transporting minute volumes of liquid. Evidence of the utility of capillary flow mediated by microchannels can be found in applications ranging from microfluidics^{1–7} to capillary micromolding^{8,9} and printed electronics manufacturing. ^{10–12}

Open microchannels (also known as microgrooves) have at least one side of the channel free, i.e., open to the atmosphere. Typical geometries feature rectangular, U'-15,19 or 'V'-10,20-22 shaped cross sections with an open top, often molded into polymer, technical etched into glass or silicon, for milled into metal. Open microchannels offer numerous advantages over their closed counterparts, including ease of fabrication (especially when printed on paper fabricated via 3D printing facilitating cleaning and air entrapment, in addition to improved access to the inside of the channel, facilitating cleaning and surface modification. While conventional pumping methods fail with respect to liquid transport in open microchannels, capillarity remains a viable, effective, and economic option.

An important feature unique to open microchannels is evaporation. Evaporation naturally accompanies the flow of volatile liquids in open microchannels and, in many applications, this evaporation is undesirable. For example, in microfluidic devices used to conduct diagnostic tests, 3,4,29 nanoliter volumes of fluid are transported around a chip and evaporation can lead to undesirable increases in solute concentration and interfere with the ultimate interpretation of the test. Similarly, devices designed to sample bodily fluids via microfluidic flow in sharp, open V-groove channels ('lancets') and also be adversely affected by evaporation.

In other applications, the evaporation accompanying capillary flow is advantageous. For example, the natural cooling associated with evaporation from open microchannels or other porous materials is often exploited in evaporative cooling devices.^{34–38} The evaporation of functional inks in open microchannels leads to coating of the channel surface. This process has been used, for example, with volatile, catalytic inks to fabricate microchannel reactors.³⁹ Electrically functional inks containing graphene,⁴⁰ conductive

polymers, ¹² silver, ¹¹ and carbon nanotubes ¹⁰ have also been flowed and dried inside of open microchannels to create printed electronic devices. Evaporation can also be used to precisely pattern colloidal particles inside of a microchannel. ⁴¹ These 'capillary coating' operations are all made possible by evaporation.

The dynamics of capillary flow in both open $^{14-17,19,24,25,42-44}$ and closed $^{14,18,45-48}$ microchannels have been studied extensively. A detailed review of these dynamics and the associated literature is provided by Ouali et al. 14 Bosanquet 49 derived an exact analytical solution for spontaneous, capillary-driven flow in horizontal closed microchannels in 1923. Others 14,15 have since extended this work to describe flow in open, horizontal channels. In the absence of evaporation, an imbibed liquid progresses through a series of flow regimes, each defined by the relationship between the position of the advancing contact line, x, and time, t. In general, this relationship can be expressed as:

$$x \propto t^n$$
 (1)

At short times $(10^{-7}-1 \text{ s}, \text{depending on the system})$, the imbibed liquid passes through inertial and transition ('visco-inertial') regimes where n gradually decreases from 1 to 0.5. In the limit of long times $(10^{-5}-10 \text{ s}, \text{ again depending on the system})$, n approaches 0.5 and the liquid enters the 'viscous' or Lucas-Washburn regime. This long-time limit represents an equilibrium balance between viscous and capillary forces and applies to most experimentally-accessible timescales; this regime is the subject of the canonical studies of Lucas and Washburn. While the predictions of Bosanquet and others have been called into question at short times due to a host of complicated and experimentally elusive nonidealities, $^{14,16,47,53-62}$ the ability of the Lucas-Washburn equation to describe capillary flow dynamics at long times in open microchannels has been demonstrated in a variety of channel architectures. 14,15,17,21

The influence of evaporation on the dynamics of capillary-driven flow remains unexplored. Those working with volatile liquids, including aqueous systems¹⁵ and various alcohols,^{17,21,63} have reported good agreement between experimental results and predictions neglecting evaporation. However, in sessile droplets of pure volatile liquid, evaporation has been shown to induce temperature gradients near the contact line.⁶⁴ These gradients have been observed to induce thermal Marangoni flows and, consequentially,

vortices within the droplet. Similar recirculation has also been observed in pure volatile liquids confined to open microtubes.⁶⁵

In volatile liquids containing solids, evaporation has a definitive influence on capillary flow behavior. Both Mahajan et al.¹¹ and Lone et al.⁴¹ note that liquids loaded with solids eventually pin permanently at the advancing contact line when flowed in a long enough channel. In both studies, this permanent pinning is attributed to the local solids concentration at the contact line exceeding some critical value, leading to local solidification and subsequent pinning at the contact line. However, in neither of these studies is the influence of drying on capillary flow dynamics investigated nor is the specific pinning mechanism explored.

In studies^{66,67} of droplets with advancing contact lines (the droplets were pushed in specialized set ups), evaporation has also been shown to increase the local solids concentration near the contact line. This is primarily attributed to the divergent evaporative flux at the contact line.^{64,68–70} This accumulation has been noted to be counteracted by hydrodynamic flow of liquid within the droplet caused by its forward motion.^{71,72} Below a certain velocity, particle accumulation exceeding a critical concentration can cause pinning of the contact line, often leading to a stick-slip motion along the substrate. This behavior has been observed in both colloidal suspensions⁶⁶ and polymer solutions.⁶⁷ In general, contact line pinning in a variety of liquid systems has been attributed to capillary forces caused by particle confinement at the contact line, which acts to resist spreading.^{73,74}

In this paper, flow and evaporation-induced drying of liquid in open microchannels is investigated quantitatively for the first time. A model system of aqueous polymer solution is studied and the effect of drying on capillary flow dynamics is explored: from when the liquid first enters the channel until the advancing contact line permanently pins $(10^{-3}-10 \text{ s})$. These capillary flow dynamics are then compared to predictions derived by Bosanquet, Lucas, and Washburn, which neglect evaporation and, as we show, fail to account for the behavior observed in our system at long times. Contact line pinning and the drying that occurs afterward $(1-10^3 \text{ s})$ are then characterized, both as a function of drying rate and channel width. An analysis of the internal flow fields within the channel that evolve as solvent leaves the system is also

included. After evaporation is complete, the resulting dry film morphology is characterized, again as a function of drying rate and channel width. In general, higher drying rates are shown to lead to increasingly dynamic pinning behavior and less uniform dry films.

This work provides insight into the capillary coating process and includes unique perspective on the influence of drying at all stages of the process, from the introduction of liquid into the channel to the formation of the final thin film. To further our investigation, the second part of this article presents two case studies with functional inks commonly used for the manufacture of printed electronics: a graphene and a poly(3,4-ethylenedioxythiophene) (PEDOT) ink. These inks are evaluated with respect to their viability in capillary coating applications, where insight is drawn from observations made with our model liquid.

Experimental

Microchannel Fabrication. Open rectangular microchannels with widths (W) ranging from 10–200 μm and a constant depth (H) of 47 μm were fabricated using a three step molding process described previously. This corresponds to a wide range of channel aspect ratios ($\varepsilon \equiv W/H$), spanning values from 0.2–4.3. Each microchannel is 30 mm long and connected to a 3-mm-diameter reservoir at one end. Microchannels were ultimately embossed in a UV-curable resin (NOA73, Norland Products, Inc., Cranbury, NJ) bonded to a glass microscope slide (75 \times 25 mm²). A schematic of the microchannel design and an SEM micrograph of a completed microchannel are shown in Figure 1. Complete fabrication details can be found in the Supporting Information.

Solution Preparation and Characterization. Aqueous solutions of poly(vinyl alcohol) (PVA; 99+% hydrolyzed, M_w = 130 kg/mol, Sigma-Aldrich Co., St. Louis, MO) with concentrations ranging from 0.03–0.12 w/w were prepared by sealing the ingredients in a gastight jar, heating overnight (14–17 h) at 97°C, and subsequently stirring until cool (~1 h). Ultrafiltered and UV-treated water (Millipore Synergy filtration system, EMD Millipore, Darmstadt, Germany) was used to prepare the solutions. All PVA solutions were used on the same day they were prepared to minimize aging effects.⁷⁵ PVA solutions with an initial concentration of 0.03 w/w were used for all flow tests.

A water-based conductive polymer solution of poly(3,4-ethylenedioxythiophene)-

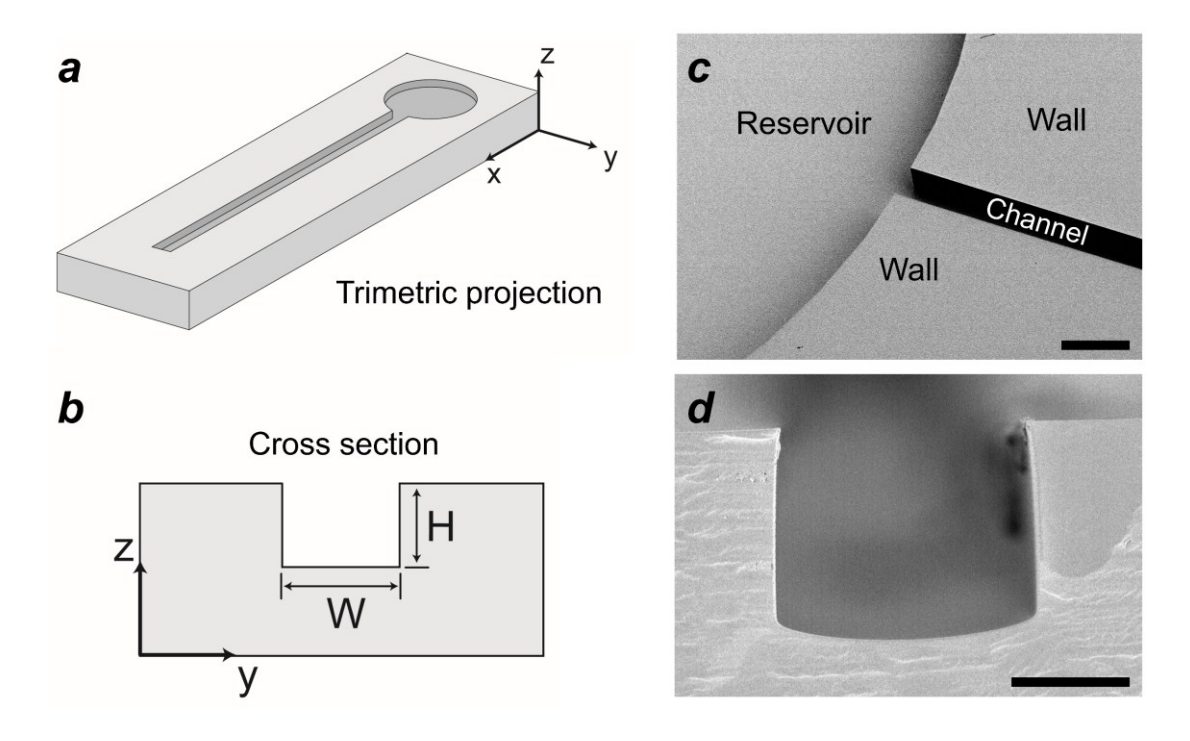


Figure 1. (a,b) Schematic of microchannel design, showing (a) trimetric projection and (b) cross section. Units in mm. Not to scale. (c,d) SEM micrographs of microchannel molded into UV-curable resin, showing (c) intersection of channel with reservoir (scale bar: 100 μm) and (d) channel cross section (scale bar: 25 μm).

poly(styrenesulfonate) (PEDOT:PSS, 0.01–0.013 w/w; Clevios PH 1000, Heraeus Holding GmbH, Hanau, Germany) was purchased commercially. A graphene ink, obtained elsewhere, ⁷⁶ was prepared by adapting methods described previously^{40,77} and consists of 15 mg/mL graphene and 15 mg/mL ethyl cellulose in a 17:3 v/v cyclohexanone:terpineol binary solvent system. The ethyl cellulose acts as a stabilizer to minimize graphene flocculation.

Physical properties and contact angles of relevant liquid systems can be found in Table 1. Viscosity was measured using a stress-controlled rheometer (AR-G2, TA Instruments, New Castle, DE) with a stainless-steel cone and plate geometry (40 mm, 2° cone angle). All aqueous PVA systems are Newtonian over a relevant range of shear rates (1–1000 s⁻¹); detailed rheological information can be found elsewhere.⁷⁸ Both the PEDOT and graphene inks are shear thinning; detailed rheological profiles can be found in the Supporting Information. Drop shape analysis (DSA-30, Krüss GmbH, Hamburg, Germany) was used to measure surface tension and equilibrium contact angle. Contact angle measurements were made on flat UV-curable resin (NOA73, Norland Products, Inc.) surfaces. To enhance wetting, surfaces used for the

measurements with aqueous PVA and the PEDOT ink were first plasma treated in air at low pressure (0.5–1 torr) for 120 s at 18 W in a plasma cleaner (PDC-32G, Harrick Plasma, Ithaca, NY). A similar procedure was used to treat all microchannel surfaces prior to any flow tests conducted with aqueous PVA or PEDOT ink. Surfaces utilized in graphene ink contact angle measurements and flow tests were not treated.

Table 1. Physical properties and contact angles of test liquids at 23°C

Sample	Density (g/cm³)	Viscosity (mPa·s)	Surface tension (mN/m)	Contact angle ^a
Poly(vinyl Alcohol) (aq.) (0.03 w/w)	1.0 ± 0.1^{b}	19 ± 1	65.0 ± 0.3	24.3 ± 0.2
PEDOT Ink	$1.0\pm0.1^{\rm b}$	$ 96 \pm 2 (1 s^{-1}) 44 \pm 1 (100 s^{-1}) $	68.7 ± 0.1	17.5 ± 0.4
Graphene Ink	0.94°	$11.7 \pm 0.1 \; (10 \; s^{-1})$ $9.4 \pm 0.1 \; (1000 \; s^{-1})$	33 ^d	~ 0

^a Measured equilibrium contact angle; ^bEstimated from gravimetric measurements with fixed volumes of liquid;

Monitoring Capillary Flow. Capillary flow was monitored using high speed video. Microchannels were first plasma treated as described above for 120 s, positioned under an optical lens (Zoom 6000 system with 3 mm FF zoom lens (Model No. 1-6232) and 2x standard adapter (Model No. 1-6030), Navitar, Rochester, NY), and illuminated with a fiber optic light. Droplets were then carefully dispensed into the center of the channel's reservoir using a syringe and needle connected to a precise and manually controlled droplet positioning system. The resulting capillary flow was recorded with a high-speed camera (Fastcam Ultima APX, Model 120 K, Photron, Tokyo, Japan) at 60–1000 fps until the advancing contact line pinned and forward motion stopped. A majority of the flow experiments were conducted at room conditions (7–50% relative humidity (RH), 23 ± 1 °C). In instances where the ambient relative humidity was not satisfactory, a humidity chamber was utilized to control the drying conditions. Details pertaining to the construction and operation of this humidity chamber are presented elsewhere.

Individual visualization experiments were limited to flow distances of 8–10 mm due to the camera's field of view. To record flow events exceeding this distance, flow behavior was recorded as a set of two videos: one recording the first 5–10 mm of flow and the second recording the final 5–10 mm of flow. Data from these two runs were then superposed by shifting the second curve laterally in time until the two curves

^c Estimated based on densities of primary solvents; ^d Based on information available in ref. ⁷⁷.

coincided. As the two recordings are made during independent trials in two different channels, this method assumes that flow behavior in separate but equivalent channels is indistinguishable. To help ensure that representative flow behavior was collected, multiple videos of both the first and second half of flow were always recorded when this two-step process was required.

Internal Flow Visualization. Flow behavior within the liquid (internal flow fields) was visualized by seeding the liquid with 2- μ m-diameter polystyrene (PS) microspheres (blue color, Phosphorex, Inc., Hopkinton, MA). Stock PS microsphere solution (0.01 v/v spheres with trace surfactant and preservative) was added to the aqueous PVA solution at a concentration of 0.06 v/v. The addition of the PS stock solution (final particle concentration $\approx 6 \times 10^{-4}$ v/v) had a negligible impact on solution viscosity but was associated with a small reduction in surface tension and equilibrium contact angle (approximately 20%). As only qualitative arguments are made here using the PS microspheres, these changes are inconsequential to the conclusions presented herein. Flow was visualized and imaged using a digital optical microscope (KH-7700 with 50–400x MX(G)-5040Z zoom lens with midrange adapter, Hirox USA, Hackensack, NJ). After contact line pinning, videos of the internal flow field were recorded as the liquid dried. Videos were taken at 1 or 2 fps over timescales of 30–600 s.

Confocal Raman Microscopy. Confocal Raman microscopy was used to measure local PVA concentration changes in select microchannels during drying. Raman spectra were collected using a confocal Raman microscope (alpha300 R with UHTS 300 ultrahigh throughput spectrometer, WITec (Wissenschaftliche Instrumente und Technologie) GmbH, Ulm, Germany) operating at an excitation wavelength of 532 nm and equipped with a motorized stage with automated positioning along all axes.

PVA has a strong, relatively narrow characteristic peak at 2910 cm⁻¹ while water has a broader peak centered around 3400 cm⁻¹. The ratio of the height of these two peaks, r_{PVA} , was correlated to a specific PVA concentration by conducting calibration experiments.⁸⁰ These calibration experiments were done by first pipetting approximately 0.5 mL of PVA solution of known concentration (0.03–0.12 w/w) onto a glass slide and gently positioning a glass cover slip onto the resulting droplet. Note that glass is not Raman active at wavenumbers of interest in this study (> 1500 cm⁻¹). Integration times of at least 5 s, averaged over at

least two accumulations, were used to obtain each spectra. The peak-to-peak height ratio (r_{PVA}), at each PVA concentration was fit to a master calibration curve with the functional form:

$$r_{PVA} \propto \frac{w}{1 - w}$$
 (2)

as suggested by Ludwig et al,⁸⁰ where w is the weight fraction of PVA in solution. This calibration curve was then corrected to account for substrate interference from the UV-curable resin, which is also Raman active around 2900 cm⁻¹. Sample Raman spectra and details on the complete calibration procedure can be found in the Supporting Information.

Raman measurements and calibration data were used to measure real-time concentration changes of PVA in open microchannels during drying. First, 100 µm wide microchannels were plasma treated for 120 s, as described above, and 0.03 w/w aqueous PVA solution was then pipetted into the channel reservoir. High flow speeds (> 1 mm/s) prohibit data collection during flow and Raman spectrographs were instead recorded after the advancing contact line had pinned. Data was collected at a fixed distance from the pinned contact line over the entire channel depth in 5 µm increments. Three spectra were recorded at each depth, spaced laterally by approximately 1 µm. Integration times of 1 s were used for all spectra recorded during drying. Shorter integration times were used here than in the calibration measurements due to the highly dynamic nature of the drying process. Relative peak height ratios are independent of integration time, but longer integration times result in spectra with less noise.

Characterizing Dry Film Morphology. Dry film morphology was measured using mechanical stylus profilometry (P-16, KLA-Tencor, Milpitas, CA) and further characterized using SEM (S-4700 cold field emission gun, Hitachi, Tokyo, Japan). Profilometry was limited to channels with $W \ge 75$ µm due to the size of the profilometer stylus. No significant difference in dry film morphology was observed between systems prepared with and without dispersed PS microspheres.

Bulk Drying Measurements. Drying behavior in each system was approximated using bulk drying measurements. Small sample volumes (\sim 50 μ L) were first placed in a shallow dish with a cross-sectional area of \sim 25 mm². Mass loss measurements were then recorded in 1 s intervals over periods of 10–

60 min. Experiments were conducted at room temperature $(23 \pm 1^{\circ}C)$ and various relative humidity levels. Additional details of these measurements and bulk drying data for each system can be found in the Supporting Information.

Results and Discussion

Capillary Flow Dynamics in the Absence of Drying. In the absence of drying, the Lucas-Washburn^{50,51} equation readily describes capillary flow behavior in horizontal microchannels:

$$x^2(t) = \frac{2b}{a}t\tag{3}$$

where x is the position of the advancing contact line and t is time. Equation 3 is valid in the limit of long times when $t \gg 1/a$. The coefficients a and b are liquid- and channel-dependent constants representing the strength of viscous and capillary forces present in the system, respectively. In open, rectangular microchannels, a and b can be approximated as:

$$a = \frac{3\eta}{0H^2} f(\varepsilon) \tag{4}$$

$$b = \frac{\gamma}{oH} [\cos \theta_e (1 + 2\varepsilon^{-1}) - 1]$$
 (5)

where ρ , η , and γ are the density, viscosity, and surface tension of the liquid system, θ_e is the equilibrium contact angle, and ε is the channel aspect ratio (W/H; see Figure 1b). (Note that θ_e in eq. 5 may not necessarily always be equal to the equilibrium value of the contact angle, and can be more generally represented by a dynamic contact angle. The geometric function f can be approximated following derivations and arguments made by Ouali et al. And Yang et al. Signature f and Yang et

$$v(t) = \sqrt{\frac{b}{2at}} \tag{6}$$

Equations 4–6 predict the existence of an optimal channel width (all other variables held constant) at which v is maximized at any given time. This optimum width is a function of the contact angle, but typically

occurs at aspect ratios close to unity.

Given the liquid properties in Table 1, initial values of a are expected to range from 10^5 – 10^6 s⁻¹. The long-time limit under which the Lucas-Washburn equation is valid is thus expected to apply at all times beyond approximately 1 ms ($1/a \approx 1$ – $10 \mu s$) for the liquids studied in this work. Given the maximum recording framerate of 1000 fps utilized in this study, all data captured beyond the first several frames should satisfy this requirement. Accordingly, n in eq. 1 is always expected to equal 0.5, corresponding to the viscous flow regime.

Capillary Flow Dynamics with Drying. Representative flow curves for spontaneous capillary filling of aqueous PVA solution in open microchannels are shown in Figures 2a and 2b. These data correspond to flow in rectangular microchannels with widths ranging from 10–200 μm and illustrate behavior at both high (7% RH) and low (80% RH) drying rates. Approximate bulk evaporation rates are indicated in each respective figure panel. Sample capillary filling events in 50 and 200 μm wide microchannels are illustrated by the image sequences in Figures 2c and 2d (at 7% RH only) and in Movies S1–S4 in the Supporting Information (at both 7 and 80% RH).

Capillary flow of aqueous PVA solution was always found to terminate with permanent contact line pinning. In Figures 2a and 2b, the transition to permanent pinning is marked with a ' $\otimes k$ ', where k equals the corresponding channel width in microns. Prior to this permanent pinning, the capillary flow can be described by one of two behaviors: (1) smooth, uniform, and unimpeded contact line motion or (2) a stick-slip motion where flow is temporarily interrupted by intermittent pinning of the contact line. The first behavior dominates at early times whereas the latter dominates at long times, often right before permanent pinning.

The drying-induced pinning illustrated in Figure 2 can be understood by drawing analogies with studies on drying droplets undergoing forced spreading, as discussed by Rio et al.⁶⁶ and Monteux et al.⁶⁷ At an advancing contact line, flow and evaporation compete with respect to the accumulation of solute (here, polymer). Hydrodynamic flow accompanying the motion of the advancing contact line continually drives upstream liquid to the contact line.⁸² This internal flow brings both solute and solvent to the contact line

and tends to homogenize the liquid in and around the moving meniscus. Oppositely, evaporation opposes this homogenization and favors solute accumulation, 66,67 especially close to the contact line where the evaporation rate diverges. 64,68,69

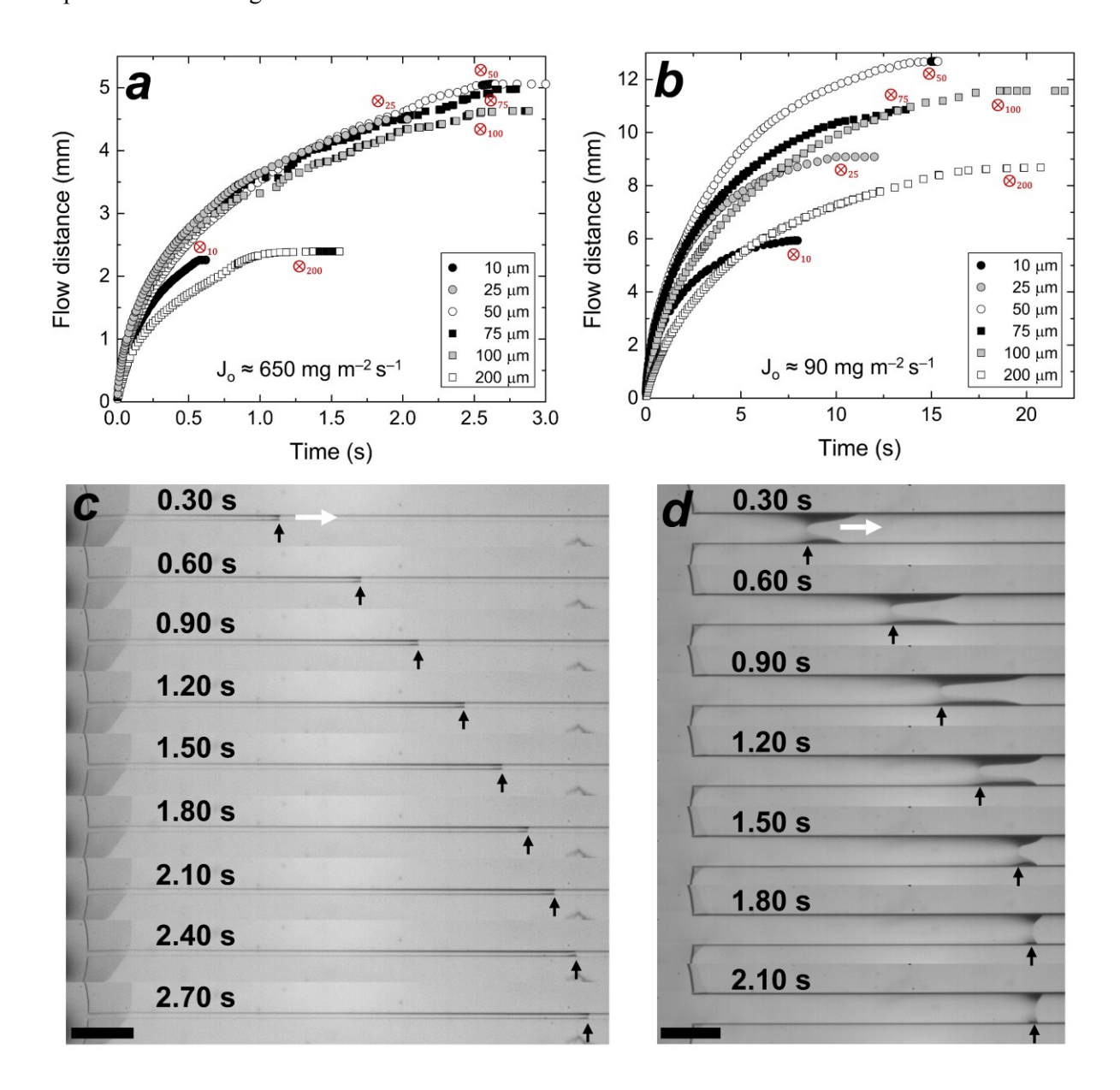


Figure 2. (a,b) Characteristic flow curves for capillary filling of aqueous poly(vinyl alcohol) (PVA) in open microchannels of indicated width at (a) 7% and (b) 80% RH. The approximate bulk evaporative flux, J_o , is indicated in each figure panel. Pinning points are indicated by ' \bigotimes_k ', where k is channel width in microns. (c,d) Image sequence of capillary filling of aqueous PVA dried at 7% RH in (c) 50 and (d) 200 μ m wide open microchannels. White arrows indicate the direction of spontaneous capillary flow and black arrows indicate the position of advancing contact line. Scale bars: 400 μ m. All channels are 47 μ m deep.

The above-described competition between hydrodynamic flow and evaporation appears to also control the capillary flow behavior shown in Figure 2. At high contact line velocities, flow-induced homogenization can outpace evaporation-induced solids accumulation and flow proceeds largely uninterrupted. This is evidenced by the relatively smooth flow curves at early times in Figures 2a (t < 0.5 s) and 2b (t < 5 s) and in Movies S3 and S4 for flow at low drying rates (80% RH). However, the physics of capillary flow dictate that velocity continually decrease as the liquid penetrates further into the channel (even when there is no drying, per eq. 6). ^{14,49–52} Accordingly, solute will necessarily build up at the contact line at long times, resulting in the inevitable transition from uninhibited flow to stick-slip behavior caused by intermittent contact line pinning. This stick-slip behavior is especially pronounced at long times (t > 1 s) in the flow curves in Figure 2a and in Movie S1. Eventually, the capillary driving force cannot surmount the pinning force and the contact line pins permanently.

Figure 3 compares capillary filling across all drying rates to that predicted for the hypothetical case of no drying (100% RH) for flow in 50 μ m wide channels. Predictions for the case of no drying are based on the initial properties of the PVA solution (see Table 1 and eqs. 3–6). At early times (t < 0.1 s), flow at all three drying rates closely follows behavior predicted for the case of no drying. Soon after these first few moments, however, the discrepancy between experimental behavior and predictions neglecting drying becomes apparent and continues to increase until the contact line permanently pins and flow abruptly stops. This discrepancy becomes more dramatic as drying rate increases.

Figure 3b plots the flow curves from Figure 3a on a log–log scale. Note that the slope of these lines is equivalent to n in eq. 1. Neglecting drying, a straight line with a slope of 0.5 (n = 0.5 in eq. 1) is expected at all times. This classic result is readily derived from eq. 3. In contrast, our experimental results show that n only transitions to 0.5 at intermediate times (0.1 < t < 0.5 s). Additionally, at long times n continues to decrease beyond the canonical 0.5 limit and is eventually driven to 0 when the contact line permanently pins. This specific long-time behavior has not been observed, to our knowledge, for any liquid flowing in a microchannel. A notable exception to this is flow in channels with rough walls, $^{27,83-85}$ where the roughness induces temporary pinning, momentarily driving velocity and n to 0. In this work, this unique behavior can

be attributed entirely to drying effects.

The discrepancy in Figure 3b between our experimental results and the predictions of eq. 3 at early times (t < 0.1 s) is consistent with the results of others^{15,18,27} and is not necessarily linked to drying. Instead, other nonidealities such as dynamic contact angle^{47,54,81} and entrance effects^{59,60} (which are especially prevalent at early times) are commonly cited as the root cause of this disagreement. While drying may exacerbate (or even mitigate) this issue, such conclusions are beyond the scope of this paper.

The instantaneous velocities associated with the flow curves in Figure 3a are shown in Figure 3c. Paired pinning-depinning ('stick-slip') events manifest themselves as rapid fluctuations in velocity; these

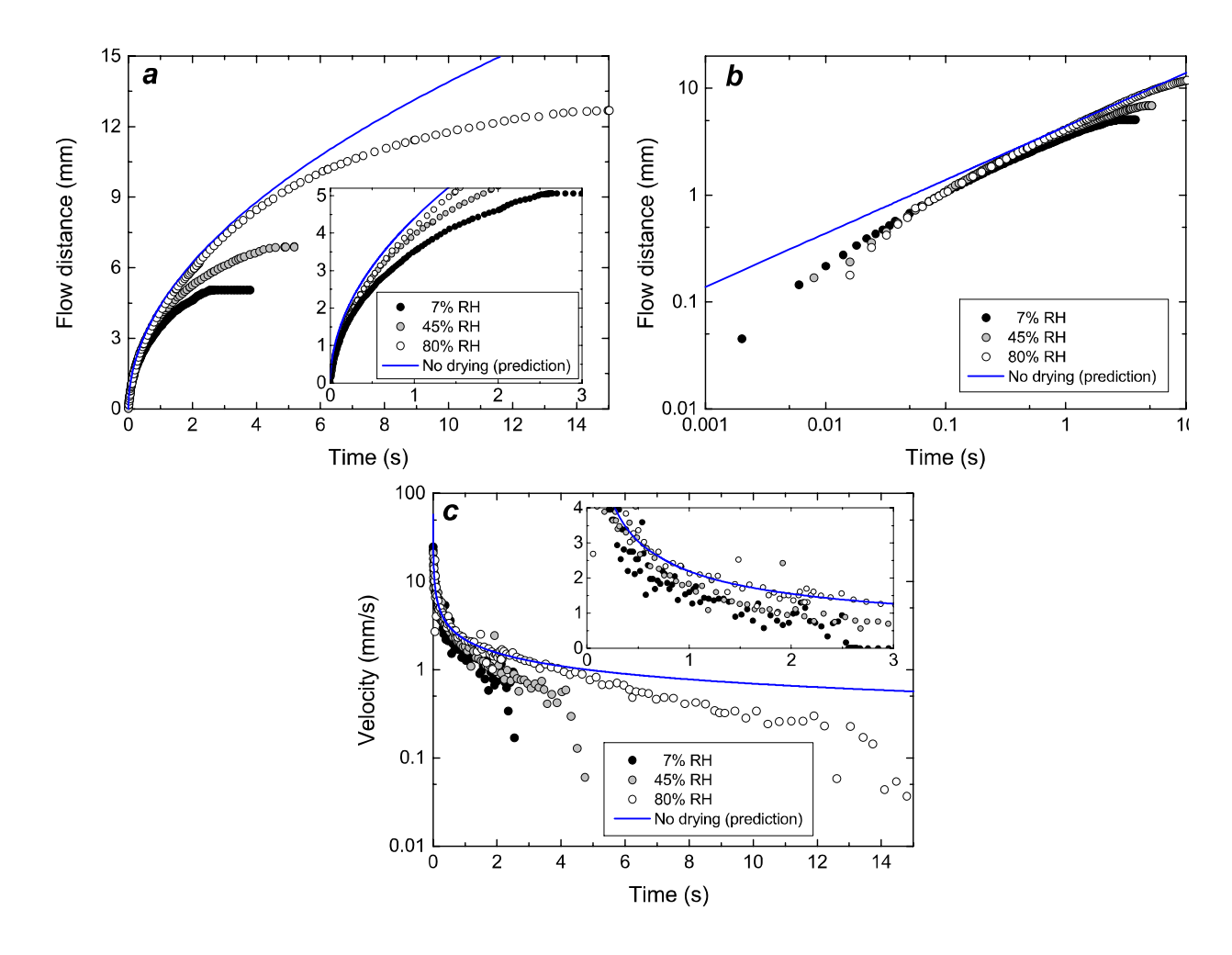


Figure 3. Comparison of capillary flow behavior at various drying rates in 50 μm wide channels. Prediction for case of no drying (100% RH) indicated by solid blue line in each panel. (a) Capillary flow curves (inset: same data expanded at early times) and (b) corresponding data plotted on log-log plot. (c) Flow velocity over time, corresponding to the data in panel a (inset: same data expanded at early times). Approximate bulk drying rates: 650, 230, and 90 mg/m²s at 7, 45, and 80% RH, respectively. All channels are 47 μm deep.

fluctuations are most apparent at high drying rates (e.g. 7% RH). The 'critical velocity,' v_c , is defined as the minimum velocity at which flow can be sustained and permanent contact line pinning occurs when $v < v_c$. (Recall that the balance between flow (a function of velocity) and drying controls solids accumulation at the contact line). While the actual magnitude of this critical pinning velocity was observed to fluctuate from run to run, higher drying rates were, on average, observed to be associated with higher critical pinning velocities. This agrees well with work on drying sessile droplets with moving contact lines. 66,67

Pinning and Stick-Slip Flow. Stick-slip flow is characterized by paired pinning-depinning events at the contact line, where motion is temporarily impeded but not permanently stopped. This behavior is caused by a significant but sub-critical solids accumulation at the contact line, which induces momentary, local solidification and temporary pinning ('sticking') to the channel. Three different types of pinning—referred to herein as types I, II, and III—are observed, each leading to a unique form of stick-slip motion.

Type I pinning events are characterized by local pinning over small (\sim 1–10 μ m) lengths of the contact line. Such a pinning event is illustrated by the image sequence in Figure 4a and by the corresponding contact line profiles in Figure 4b (compare the profiles from 5–15 ms at an x-y coordinate of 30 x 40 μ m). This localized, rapid pinning is likely induced by small imperfections on the microchannel surface that act to locally impede (pin) contact line motion. Such an effect is expected to be accentuated at long times, induced by the higher viscosity associated with extended drying. Random fluctuations in contact line shape during flow, however slight, could also lead to inhomogeneous drying. This in turn could lead to local fluctuations in solids concentration and, accordingly, isolated pinning events.

Despite local pinning, capillarity continues to drive flow down the channel and all unpinned portions of the contact line remain mobile. At the (stationary) pinning site, this flow acts to locally increase the contact angle, θ , analogous to the behavior exhibited by advancing contact lines on rough surfaces. As shown by others, 88,89 a contact line with $\theta > \theta_e$ exists in an unstable state (θ_e is the equilibrium contact angle) and beyond a critical contact angle, the contact line will depin. This critical point is dictated by the strength of the liquid-solid interaction. Beyond increasing the local contact angle, hydrodynamic motion in the vicinity of the pinning site will also tend to homogenize the local polymer concentration and eliminate

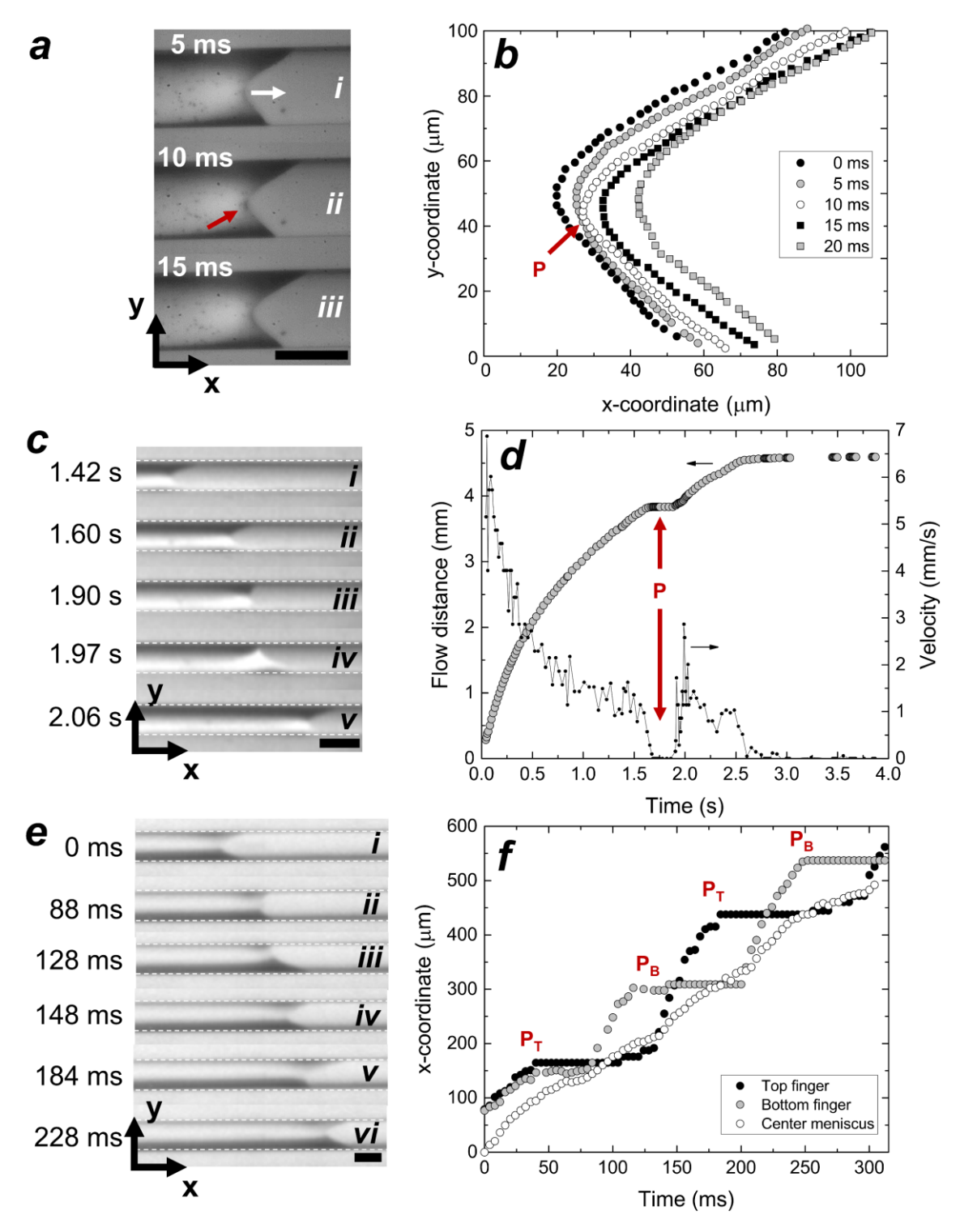


Figure 4. (a) Image sequence and (b) corresponding contact line profiles for type I pinning event. PS tracer particles are present. (c) Image sequence and (d) corresponding flow distance and velocity versus time for type II pinning event. (e) Image sequence and (f) corresponding position of the contact line, by location (top, bottom, or center) for type III pinning event. P_T and P_B indicate pinning points of the top or bottom finger, respectively. In panels a, b, and d, pinning sites are marked by a "P" and/or a dark arrow. In panels b, d, and f, time is relative to an arbitrary zero point. In panels c and e, white dashed lines denote channel walls. All channels are 100 μm wide and 47 μm deep. All scale bars: 100 μm.

regions of high solids content, further assisting with depinning. Upon depinning, the contact line rapidly jumps forward and (provided it does not immediately pin again) quickly resumes its pre-pinning shape, ⁸⁹ as illustrated in Figure 4b (t = 10-15 ms). Type I pinning events were observed to last on the order of 5–10 ms. However, clusters of type I pinning can lead to pinning over larger length scales, which is associated with longer depinning times or even permanent contact line pinning.

Type II and III pinning events are physically similar to type I events but refer specifically to pinning of the liquid 'fingers'. Liquid fingers—sometimes called Concus-Finn filaments⁹⁰—are local, permanent distortions in contact line shape formed due to the low Laplace pressure in the corners of the channel.^{13,43,91,92} These distortions are readily apparent in Figure 2d and are characterized by the wedge-shaped 'fingers' of liquid extending ahead of the main meniscus. In Figures 2c and 2d, these fingers can be found to the right of the black vertical arrows. Fingers were observed to form in channels of all widths, but were largest (longest) in wider channels (compare Figures 2c and 2d). In 100 and 200 μm wide channels, the length of these fingers was even observed to grow over time. The formation of liquid fingers in rectangular channels is a well-documented phenomenon^{14,16} and is expected when working with any wetting liquid. The observed dependence of finger length on channel width is consistent with observations by others.^{15,16}

The morphology and relative isolation of the fingers from the rest of the contact line compels them to dry and pin first, before other portions of the contact line. A type II pinning event is characterized by temporary and simultaneous pinning of both fingers. An example of type II pinning and the associated stick-slip motion is illustrated by the image sequence in Figure 4c and Movie S5 in the Supporting Information; the corresponding contact line position and velocity over time are presented in Figure 4d. When both fingers pin simultaneously (Figure 4c(ii)), they anchor the edges of the contact line while the central meniscus continues to flow forward until the contact line is nearly flat across the channel (Figure 4c(iii)). This corresponds to a dramatic reduction in the flow velocity from 1.6 to 1.9 s in Figure 4d.

By similar depinning mechanisms described above for type I events, the fingers eventually depin and the contact line quickly pulses forward (Figure 4c(iv-v)). This corresponds to the rapid increase in

velocity at t = 1.9 s in Figure 4d. Typical timescales for type II pinning events are on the order of 100–500 ms, with longer times associated with larger (longer) fingers (i.e., wider channels). If the fingers anchor too strongly to the walls, a type II pinning event can permanently pin the contact line (e.g., see Figure 2b).

Type III pinning events occur when one finger pins independently from the other. This results in one half of the contact line becoming 'anchored' to the channel. Flow of the other half of the contact line (including the second finger) down the channel contributes to depinning by mechanisms described above for type I pinning events. If the anchored finger is only weakly pinned, flow continues unimpeded after depinning and the event can be considered 'isolated'. This behavior is most commonly observed at early times. At later times, depinning of one finger is often followed by the immediate pinning of the other. The increased likelihood of subsequent pinning by the second finger can be attributed to the extension that it undergoes while the other finger is pinned. This extension causes thinning, accelerated drying, and, in turn, increases the likelihood of pinning. The originally pinned finger now resumes flow but remains partially constrained by the other (now-pinned) finger.

Figure 4e illustrates the stick-slip motion associated with repeated type III pinning events. The corresponding x-coordinates of each finger and the center of the contact line are shown in Figure 4f. At early times (t < 40 ms), the fingers move together, approximately 80 μ m ahead of the central contact line. At $t \approx 50$ ms, a type II pinning event momentarily pins both fingers. At $t \approx 90$ ms (Figure 4e(ii-iii)), the bottom finger depins while the top finger remains pinned. The bottom finger continues to move down the channel for 40 ms, extending approximately 150 μ m past the top finger (Figure 4e(iii)). The bottom finger then pins, followed by depinning of the top finger, which travels past the now-pinned bottom finger as it moves from $t \approx 200$ to 450 $t \approx 200$ to 450 mm (Figure 4e($t \approx 200$)). This process repeats as the top finger pins again, followed by depinning of the bottom finger (Figure 4e($t \approx 200$)).

As Figures 4e and 4f illustrate, the pinning of a single finger can act to destabilize the motion of the entire contact line and cause it to 'crawl' down the channel. This crawling cycle often repeats until one finger pins permanently, eventually arresting all forward motion. A cartoon and video (Movie S6) of the above-described behavior are presented in the Supporting Information.

The specific balance between type I, II, and III pinning events in our channels was found to strongly depend on drying rate. Higher drying rates were observed to be associated with a highly dynamic stick-slip flow and an increased occurrence of repeating type III pinning events (crawling behavior). Oppositely, lower drying rates were found to be most conducive to a more gradual deceleration of flow, promoting isolated pinning events of all types. Channel width was also found to play a role in the specific pinning behavior observed and intermediate channel widths (50 μ m $\leq W \leq$ 100 μ m) were most often associated with repeated stick-slip behavior, caused primarily by type III pinning events. Oppositely, very wide (200 μm) and very narrow (10 µm) channels were rarely associated with any stick-slip behavior. The above-described dependencies are explored in more detail in the Supporting Information. **Total Flow Time** and Distance. Figure 5 summarizes total flow times and distances for all combinations of channel width and drying rate. Total flow time (Figure 5a) increases with channel width until a drying rate-dependent critical value, Wc, which increases as drying rate decreases. At 80% RH, total flow time continues to increase up to the maximum channel width tested (200 µm). The corresponding total flow distances in Figure 5b are maximized at channel widths between 50 and 100 μ m ($\varepsilon = 1.1-2.1$) regardless of drying rate. Lower drying rates are always associated with longer flow distances and times at any given channel width.

Channel width influences total flow time by controlling two key parameters: contact line velocity and contact line morphology. Higher contact line velocities result in increased flow to the contact line, lending an increased resistance to evaporation-induced pinning and promoting longer total flow times. This direct relationship between contact line velocity and flow to the contact line has been demonstrated by others⁸² and also independently verified for our own system using 2 μ m tracer particles (see Supporting Information). Using the physical properties reported in Table 1 for our PVA system and neglecting drying effects, eqs. 4–6 predict maximum flow velocities at widths of 50 μ m (all other variables held constant). As width decreases below 50 μ m, flow velocity is predicted to drop off steeply due to dramatically increased viscous resistance. This explains the behavior observed in Figure 5a when $W \le 50 \mu$ m.

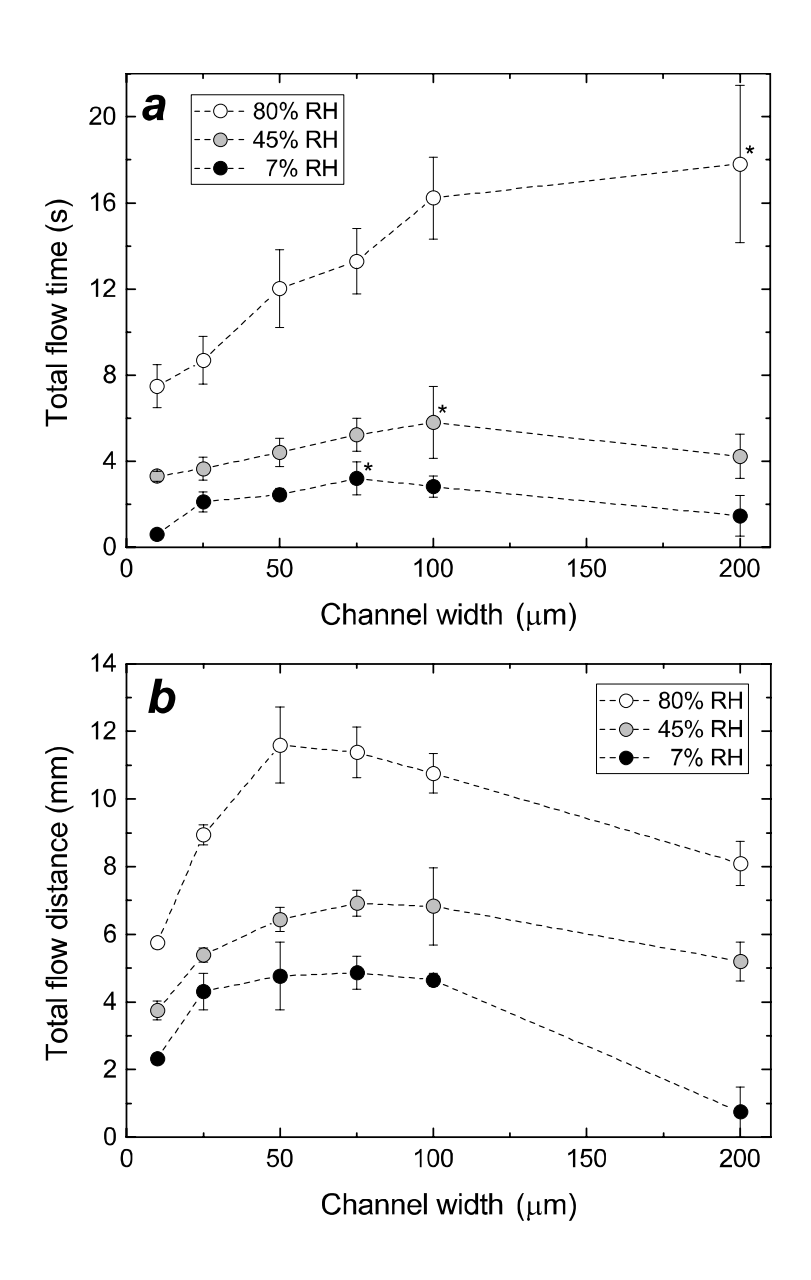


Figure 5. Average (a) total flow times and (b) total flow distances associated with flow of aqueous poly(vinyl alcohol) (PVA) in open microchannels as a function of channel width and indicated relative humidity. In (a), asterisks (*) mark the critical channel width, W_c . Data represent averages measured from 3–10 individual trials and error bars represent 90% confidence intervals. Approximate bulk drying rates: 650, 230, and 90 mg/m²s at 7, 45, and 80% RH, respectively. All channels are 47 µm deep.

The reasoning above, however, fails to account for the continued increase in total flow time at widths beyond 50 µm in Figure 5a. To explain this behavior, contact line morphology must be considered. As discussed above, the liquid fingers dry relatively quickly and act as anchoring points. As channel width is increased, the distance between these anchoring points increases, the central contact line can remain fluid longer, and permanent pinning is delayed. At 7 and 45% RH, this effect appears to offset effects of

decreasing flow velocity and total flow time remains relatively constant over widths of 50 to 100 µm. At 80% RH, this effect is significant enough to increase total flow time by 30% over the same width range.

Increasing channel width beyond 50 μ m can thus extend total flow time. However, this improvement is limited; the cutoff for this limit was defined previously as the critical channel width (W_c). As Figure 5a reveals, higher drying rates are associated with lower values of W_c while slow drying rates afford even very wide channels long flow times. This suggests that flow at high drying rates relies heavily on the homogenization induced by contact line motion (i.e., high velocities are important). These high velocities are necessary to compensate for the large evaporation rate at the contact line. At lower drying rates, drying at the contact line can be counteracted by comparatively low flow velocities and the benefits of increasing channel width are accentuated.

Total flow distance (Figure 5b) is simply the product of the total flow time and the average flow velocity. As discussed, flow velocity is maximized when $W \approx 50~\mu m$ (in the absence of drying). Accordingly, total flow distance increases with channel width from 10 to 50 μm at all drying rates because both average flow velocity *and* total flow time increase. When $W > 50~\mu m$, longer total flow times compensate for lower average flow velocities and total flow distance in 50, 75, and 100 μm wide channels are comparable at all drying rates. When $W = 200~\mu m$, however, the greatly reduced flow velocity always results in a reduction in total flow distance. Similar trends in total flow distance have been observed by Mahajan et al., ¹¹ who monitored the flow of volatile silver ink⁹³ in open rectangular microchannels with a wide range of aspect ratios.

Drying After Permanent Pinning. After the advancing contact line permanently pins, internal flow continues within the liquid confined between the pinned contact line and the reservoir. Visualizations of this internal flow field are presented in Figures 6a and 6b. Each image comprises multiple superimposed images taken 1 s apart at various times after permanent contact line pinning. Visualization of the flow is made possible by 2 µm tracer particles in the solution. A video of the flows corresponding to Figures 6a and 6b can be found in Movie S7 in the Supporting Information.

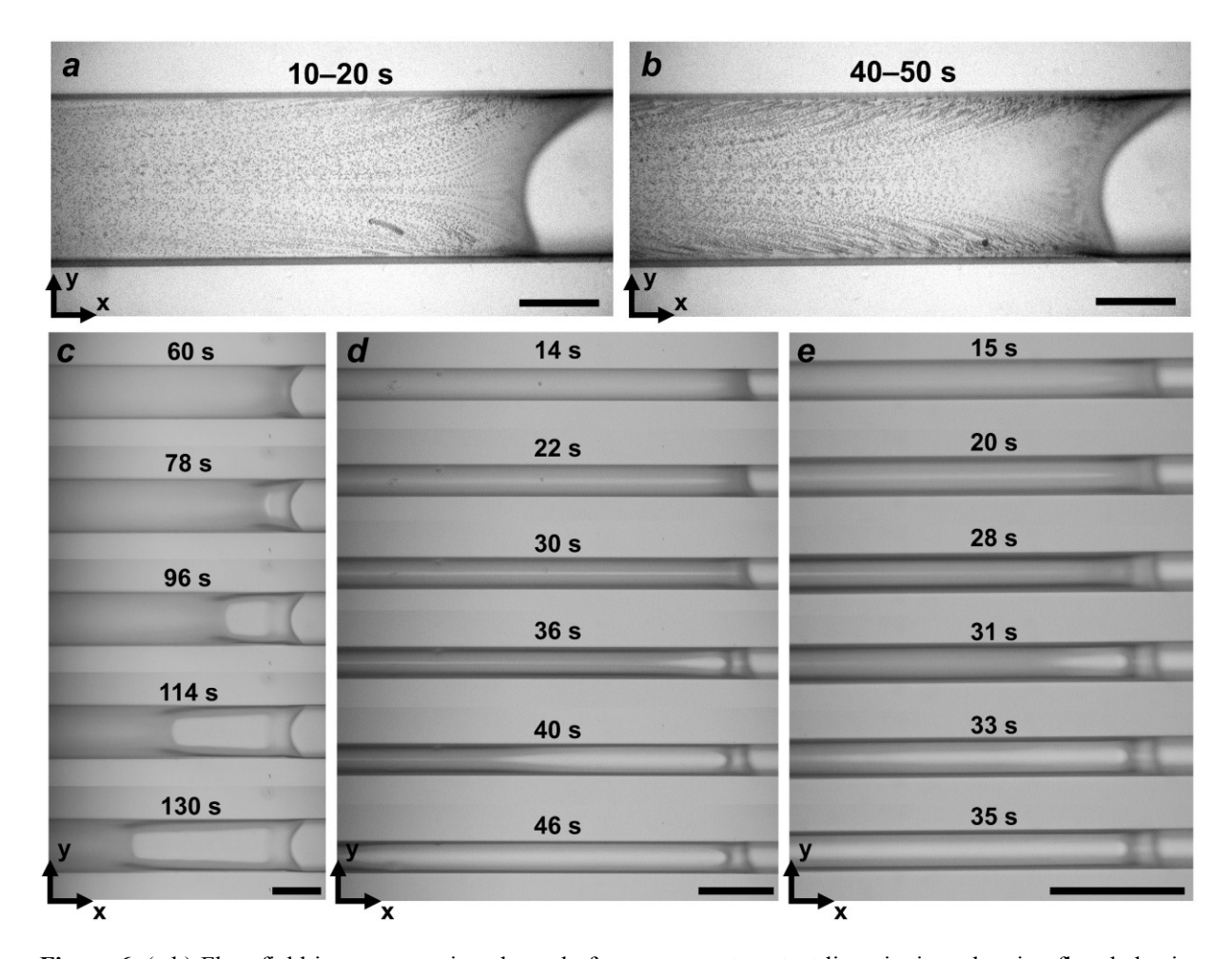


Figure 6. (a,b) Flow field in an open microchannel after permanent contact line pinning, showing flow behavior from (a) 10–20 s and (d) 40–50 s.. Each image consists of 10 superposed images, spaced 1 s apart. (c-e) Image sequences illustrating motion of drying front in (a) 200, (b) 75, and (c) 50 μm wide open microchannels. In each panel, the drying front moves from right (at the pinned contact line) to left (toward the reservoir (not shown)). RH $\approx 10\%$. All channels are 47 μm deep. Scale bars: (a,b) 100 μm , (c-e) 200 μm .

Post-pinning flow is dominated by motion along the x-axis, toward the primary (previously advancing) contact line, but there is also a small lateral velocity along the y-axis toward each wall (where two secondary contact lines form where the liquid pins to the upper edge of each sidewall). In the center of the channel (y = 0), fluid flows nearly uniaxially while liquid further from the center ($y \to W/2$) is increasingly likely to drift toward the walls. Close to the primary contact line, nearly all of the liquid is drawn into the fingers. At early times (relative to the time of pinning; Figure 6a), uniaxial motion along the x-axis dominates, but at later times (Figure 6b) this movement is diminished as the region of influence near the walls gradually increases due to drying at the secondary contact lines.

Post-pinning internal flow along the x-axis is caused by the uneven evaporative flux over the liquid

surface. Specifically, the evaporation rate is higher near the contact line than further back in the channel, analogous to the scenario that exists over an evaporating, sessile droplet with a pinned contact line. ^{64,68,69} Also analogous to the behavior observed in sessile droplets, this uneven evaporative flux induces convective flows toward the pinned contact line. This phenomenon is generally referred to as the coffee ring effect. ^{68,69} The lateral internal flows along the *y*-axis are generated by the pinning of the liquid to the top edge of each wall. As noted by others, ^{94,95} drying liquids confined by walls tend to pin to the top of those walls and, as drying proceeds, that pinning persists. To compensate for evaporation at the pinned edges, outward lateral flows are generated from the center of the channel. ⁹⁵ This effect is enhanced by (but not dependent on) the larger evaporation rate at the walls (compared to that in the center of the channel). ^{65,94} Similar motion is observed by Lone et al. ⁴¹ in drying colloidal suspensions confined in open microchannels.

The velocity of this internal flow was observed to vary with both time and drying rate, but was consistently on the order of $\sim 1-10~\mu m/s$. In general, the highest velocities were observed at early times, gradually decreasing as drying progressed and viscosity increased. Larger drying rates were observed to promote higher flow velocities, presumably due to the increased evaporative flux at the contact line driven by the lower humidity level.

As drying continues, a drying front forms at and propagates upstream from the primary (pinned) contact line. As the drying front progresses, the internal flow described above persists and polymer continues to be driven to the (now mobile) drying front. Drying front behavior as a function of channel width is shown in the image sequences in Figures 6c–6e and at the end of Movie S7 in the Supporting Information. In a 200 µm wide channel (Figure 6c), the drying front is characterized by a distinct, translucent region propagating along the *x*-axis toward the reservoir. As channel width decreases, the drying front loses it 'sharpness' but moves at a higher velocity. This is illustrated by the image sequence in Figure 6d for drying in a 75 µm wide channel. In a 50 µm wide channel (Figure 6e), the drying front loses its sharpness and instead a diffuse 'front' travels rapidly backward toward the reservoir.

Drying at the channel sidewalls influences how the drying front velocity and its 'sharpness' vary with channel width. As at the primary contact line, the drying rate at the sidewalls is higher than in the

center of the channel.^{65,94} As channel width increases, this edge drying contributes less to the removal of solvent upstream of the pinned contact line and a larger PVA concentration gradient forms across the drying front (evidence for this large concentration gradient is shown in Figure 7). As shown by others, ^{96,97} larger concentration gradients result in slower front velocities. Here, this behavior is also associated with a more distinct drying front. As channel width decreases, edge drying becomes more significant, the concentration gradient across the front decreases, and front velocity is increased. A more uniform solids concentration within the channel also leads to a broadening of the drying front and a more diffuse appearance.

To characterize the nature of the drying front more quantitatively, confocal Raman microscopy was used to monitor local PVA concentration changes over time. Figure 7a shows this behavior at fixed distances of 0.01, 1.5, and 3.5 mm from the pinned, primary contact line during drying in a 100 μm wide channel. The sharp increases in PVA concentration at 60, 400, and 1000 s correspond to the drying front passing these three observation points, respectively. This was confirmed by switching the confocal microscope between Raman and optical modes quickly during measurement. As the drying front passes each point, the concentration rises quickly up to approximately 0.70 w/w, corresponding to a solids volume fraction of approximately 0.65. After the drying front passes, the local evaporation rate drops precipitously and the remaining solvent leaves the system very slowly. Further upstream, the concentration of polymer remains relatively low until the drying front passes. This agrees well with predictions in drying thin films. 98

Approximate film thicknesses during drying can also be extracted from the confocal Raman measurements. The location of the liquid-air interface can be approximated by noting where the Raman signal switches from in focus to out of focus. These measurements are shown in Figure 7b, measured at a constant distance of 1.5 mm from the primary contact line in the center of the channel. Before the drying front passes, film thickness is relatively constant at around 40 μm. This thickness is slightly smaller than the total channel depth (47 μm) due to the curvature of the meniscus along the *y*-axis. As the drying front passes, film thickness rapidly decreases from 40 to 15 μm and then gradually decreases to 5 μm. Similar thickness changes are expected regardless of distance from the pinned contact line (except very close to the contact line, as discussed in the next section).

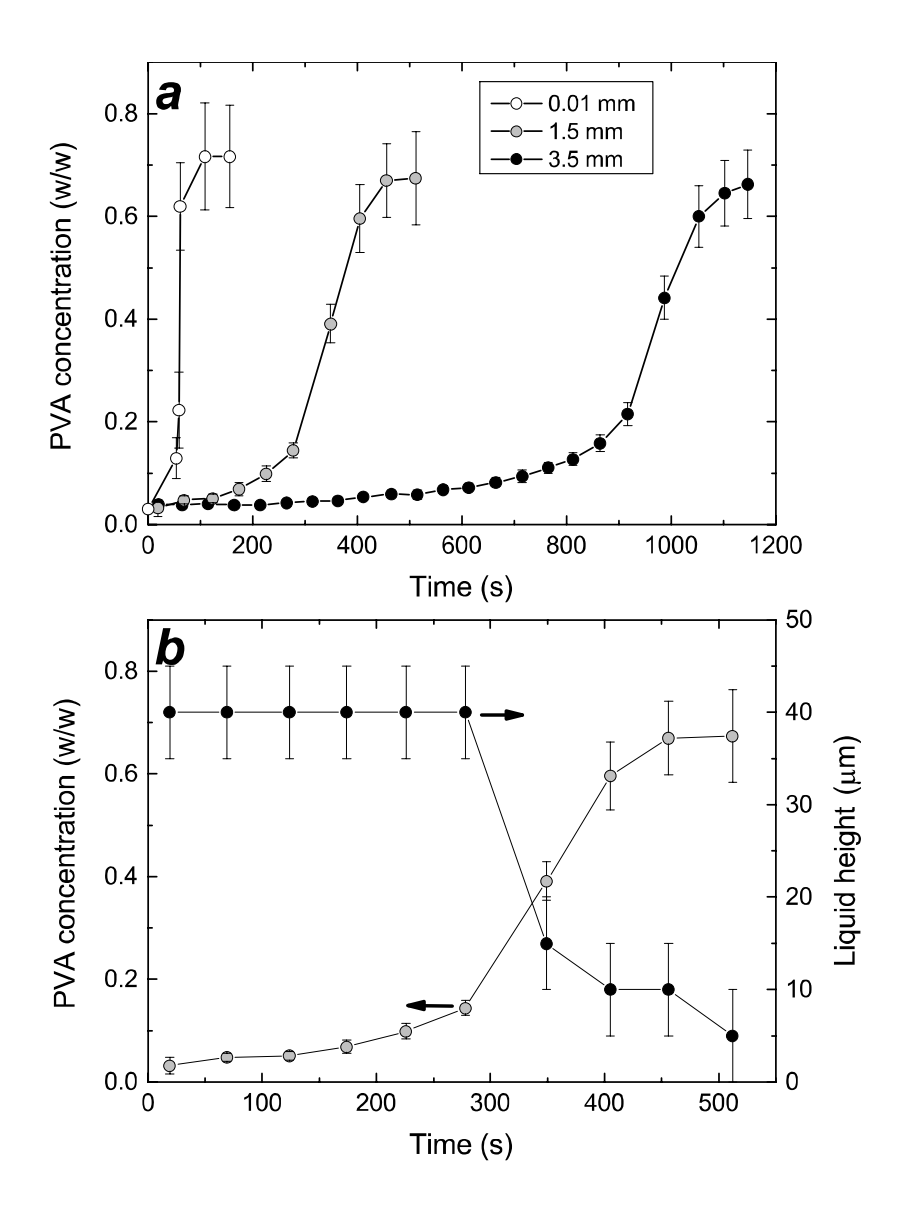


Figure 7. (a) Poly(vinyl alcohol) (PVA) concentration over time at indicated distances from the pinned contact line. (b) PVA concentration over time at a fixed distance of 1.5 mm from the pinned contact line and corresponding thickness change of liquid in microchannel (measured in center of channel). The uncertainty in thickness is equal to one half of the vertical distance between consecutive measurements: \pm 2.5 μ m. Due to the proximity of the microscope lens to the channel during drying, the effective (local) relative humidity level applicable to these experiments may be higher than the actual humidity level of the room in which the measurements were made (~50% RH). All channels are 100 μ m wide and 47 μ m deep.

Dry Film Morphology. The internal flow described in the previous section results in the accumulation of solute at all contact lines. Profilometer scans taken over the primary contact line (along the *x*-axis) after drying are shown as a function of drying rate and channel width in Figures 8a and 8b, respectively. As drying rate increases, so does the accumulation of polymer at the contact line. This is due to an increased flow rate of solute to the drying front, driven by the overall higher evaporative flux.

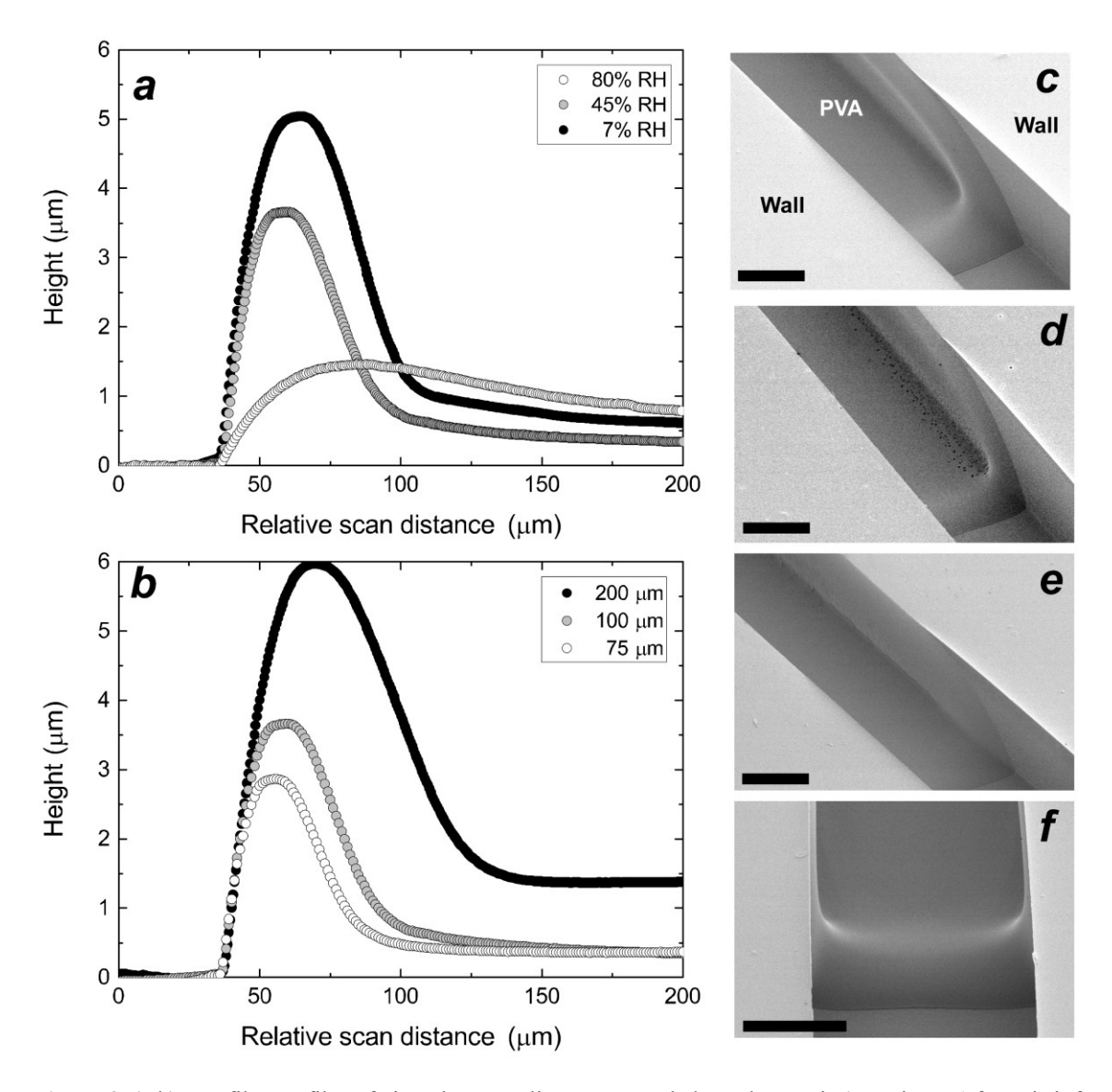


Figure 8. (a,b) Dry film profiles of pinned contact lines measured along the *x*-axis (see Figure 1 for axis information) showing the effect of (a) drying rate ($W = 100 \mu m$) and (b) channel width (RH = 45%). All profiles have been shifted laterally so that the front of the contact line begins at ~40 μm . Actual total flow distances corresponding to each profile can be found in Figure 5. (c–f) SEM micrographs of dry films in 50 μm wide microchannels dried at (c,f) 7% RH, (d) 45% RH, and (e) 80% RH. Panels c–e show dry film morphology from an oblique angle. Panel f shows dry film morphology as viewed directly in front of the dry contact line. In panel d, black dots on the dry PVA film are artifacts of air bubbles trapped during flow. All channels are 47 μm deep. All scale bars: 25 μm .

Although higher drying rates lead to less total time for accumulation, higher flow velocities caused by the increased evaporative flux appear to overcompensate for the reduced drying time. Larger channel widths are associated with a more pronounced local accumulation, as illustrated in Figure 8b. This can be attributed to the longer 'open times' promoted by wider channels. That is, wider channels foster longer times between

permanent contact line pinning and formation of the drying front (which arrests flow to the contact line), as illustrated by the image sequences in Figures 6c–6e.

Figures 8c–8f illustrate how dry film morphology varies as a function of drying rate, revealing accumulation of polymer at *all* contact lines. These results agree qualitatively with those shown in Figure 8a, but also reveal that a significant amount of material accumulates near the sidewalls due to lateral flow along the *y*-axis. This accumulation at the walls is also more pronounced at higher drying rates.

Case Studies in Printed Electronics. In this section, we seek to extend observations made on aqueous PVA solutions in the first part of this article to more complex systems. Specifically, this section presents case studies of electrically functional inks based on PEDOT and graphene. The goal of this comparison is to gain insight into how these functional inks flow, pin, and dry in open microchannels. This information will help identify key strengths and limitations of these inks with respect to their ability to effectively form capillary coatings.

PEDOT Ink. Relevant physical properties of the PEDOT ink are listed in Table 1 along with its measured equilibrium contact angle. Representative flow curves for capillary filling of the PEDOT ink in channels with widths ranging from 10–200 μm are shown in Figure 9a. Instantaneous velocities associated with flow in the 50 and 100 μm wide channels are shown in Figure 9b and average total flow distances and times are reported in Figure 9c. Drying conditions are reported in the Figure 9 caption.

Flow of the PEDOT ink is characterized by three distinct features: minimal stick-slip behavior, low velocities just before pinning, and a large critical channel width ($W_c \ge 200 \mu m$, per Figure 9c). The mild stick-slip behavior and resulting smooth flow of the PEDOT ink is evidenced by the visually smooth curves in Figures 9a and 9b. In Figure 9b, permanent contact line pinning occurs at velocities of approximately 20 and 35 $\mu m/s$ for flow in the 50 and 100 μm wide channels, respectively. These are both 60–80% lower than pinning velocities observed with the aqueous PVA solution under similar drying conditions (approximately 170 and 100 $\mu m/s$ in 50 and 100 μm wide channels, respectively).

The above-described behavior is reminiscent of that for aqueous PVA dried at the lowest rate ($J_o \approx$ 90 mg/m²s, 80% RH). However, the Figure 9 caption reveals that the approximate bulk evaporative flux

measured for the PEDOT ink ($J_o \approx 530 \text{ mg/m}^2\text{s}$) closely matches that observed in aqueous PVA when dried at the *highest* rate ($J_o \approx 650 \text{ mg/m}^2\text{s}$, 7% RH). This disparity suggests that under equivalent drying conditions, PEDOT is more resistant to contact line pinning than aqueous PVA. This follows from arguments made earlier when comparing flow behavior of aqueous PVA dried at 7% and 80% RH.

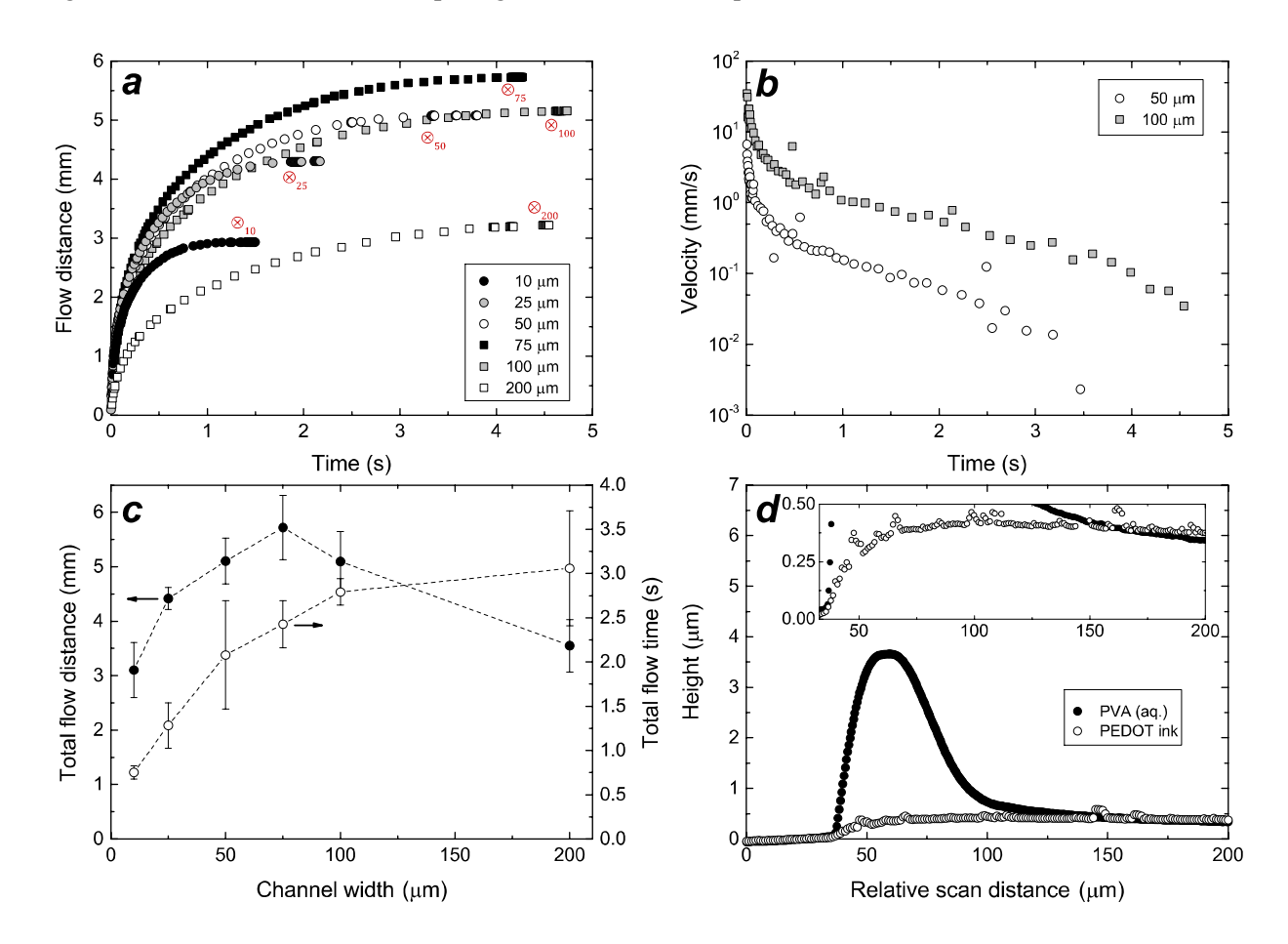


Figure 9. (a–c) Capillary filling behavior of PEDOT ink (13% RH, 23°C, $J_o \approx 530$ mg/m²s). (a) Characteristic flow curves for indicated channel widths, (b) instantaneous velocities for flow in channels of indicated width (corresponds to data in panel a), and (c) average total flow times and distances as a function of channel width. In (a), pinning points are indicated by ' \bigotimes_k ', where k is channel width in microns. (d) Dry film morphology of PEDOT ink and aqueous poly(vinyl alcohol) (PVA) solution dried in a 100 μm wide channel at 45% RH. Inset shows same data enlarged at small heights. All profiles have been shifted so that the front of the contact line begins at approximately 40 μm. Actual flow distances corresponding to each profile can be found in Figure 5b or 9c. All channels are 47 μm deep.

The decreased 'pinnability' of the PEDOT ink can be primarily attributed to a combination of two effects. First, PEDOT:PSS is known to gel in solution and the same PEDOT ink as is used in this study has been shown to form gel particles as large as 600 nm. ⁹⁹ This is dramatically larger than the ~17 nm radius of gyration (R_g) estimated for the polymer molecules in the aqueous PVA solution used here. ¹⁰⁰ Rio et al. ⁶⁶

estimate that the velocity below which an advancing contact line will pin is inversely proportional to the square root of the diameter of the particles in the solution. Hence, smaller particles are expected to be associated with pinning at higher velocities (i.e., increased 'pinnability'). Second, the initial solids concentration of the PEDOT ink is ~0.013 w/w compared to the 0.03 w/w PVA solution concentration. Work by Rio et al. also shows that decreased initial solids concentrations are expected to decrease the pinning velocity of the advancing contact line. This argument is supported by details presented earlier; namely, that the balance between flow to the contact line and evaporation dictates how quickly solids accumulate at the contact line. Given a constant evaporation rate, it stands to reason that a higher bulk solids concentration is more conducive to a critical accumulation of solids at the contact line.

Non-Newtonian rheology (shear-thinning; see Figure S1 in the Supporting Information) may also play a role in the unique flow behavior observed in the PEDOT ink. As noted by others, ¹⁰¹ shear thinning liquids flow faster at early times in capillary channels than comparable Newtonian liquids due to the drop in viscosity with increasing shear rate. As discussed above, lower viscosities can enhance hydrodynamic flow (especially near the contact line) and deter pinning.

After permanent contact line pinning, the internal flow field in the PEDOT ink is very similar to that observed in the aqueous PVA system (Figures 6a and 6b). However, the drying front forms much sooner in the PEDOT ink than in the aqueous PVA system. For example, in a 200 µm wide channel at 10% RH, a drying front forms approximately 10 s after permanent pinning of the PEDOT ink as compared with 50 s after permanent pinning of the aqueous PVA solution. This rapid drying front formation may be caused by gelling of the PEDOT during drying, which can occur at concentrations as low as 0.02 w/w. This greatly reduced open time results in a significantly diminished overall buildup of material at the contact line by the coffee ring effect. This is apparent from the dry film profiles shown in Figure 9d, comparing the final dry film morphology of the PEDOT ink and the aqueous PVA solution in a 100 µm wide channel.

Graphene Ink. Relevant physical properties of the graphene ink are listed in Table 1 along with its measured equilibrium contact angle. Average total flow times and distances for capillary filling of graphene ink in microchannels with widths ranging from 10–200 μm are summarized in Figure 10a. Figure

10b shows a characteristic flow curve for capillary filling in a 50 µm wide channel and Figure 10c shows the associated instantaneous velocity versus time. Drying conditions are reported in the Figure 10 caption.

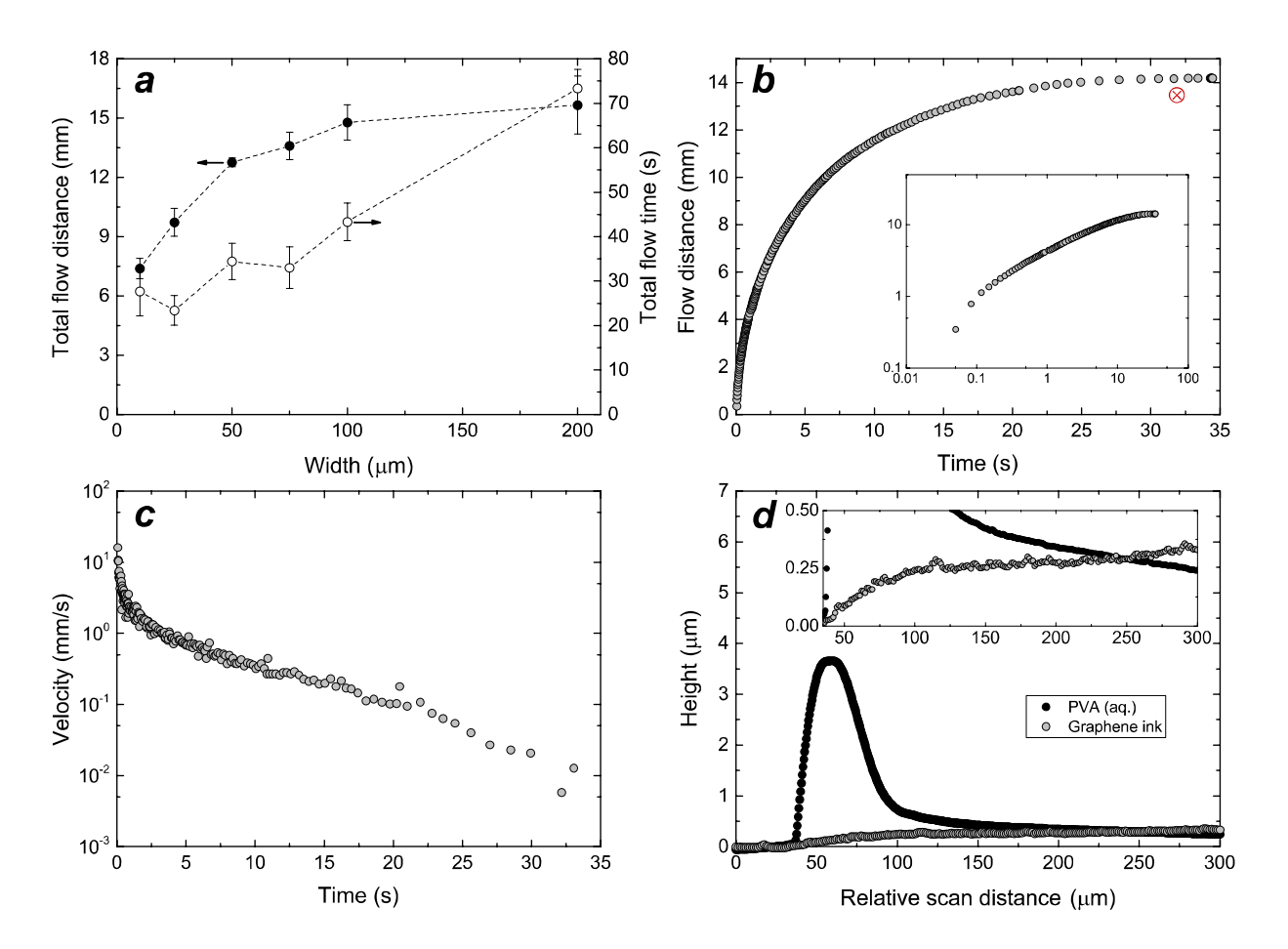


Figure 10. (a–c) Capillary filling behavior of graphene ink (30% RH, 23°C, $J_o \approx 90 \text{ mg/m}^2\text{s}$). (a) Average total flow times and distances as a function of channel width, (b) characteristic flow curve for 50 μm wide channel (inset: same data, log-log scale), and (c) instantaneous velocity for flow in 50 μm wide channel (corresponds to data in panel b). In (b), pinning point is indicated by '⊗.' (d) Dry film morphology of graphene ink and aqueous poly(vinyl alcohol) (PVA) solution dried in 100 μm wide channel at 45% RH. Inset shows same data enlarged at small heights. All profiles have been shifted so that the front of the contact line begins at approximately 40 μm. Actual flow distances corresponding to each profile can be found in Figure 5b or 10a. All channels are 47 μm deep.

Flow distances and times exhibited by the graphene ink far surpass those observed among both the aqueous PVA system and PEDOT ink. Even the shortest flow time in Figure 10a (~20 s) exceeds the longest flow time exhibited by the aqueous PVA system at any drying rate. Similar to the PEDOT ink, the behavior of the graphene ink most closely mirrors that observed with aqueous PVA at the lowest drying rate. In addition to the long flow distances and times, the graphene ink exhibited very little stick-slip behavior, low

velocities at pinning ($\sim 10~\mu m/s$ from Figure 10c), and a large critical channel width ($W_c \approx 200~\mu m$).

The comparisons made above parallel those made earlier between the PEDOT ink and the aqueous PVA system. However, unlike the large PEDOT:PSS gel particles, the graphene sheets utilized in this study are more similar in size to the PVA molecules: approximately 50 x 50 nm² with thicknesses of 2 nm⁷⁷ (compared to $R_g \approx 17$ nm for the PVA molecules, as discussed above). Further, the graphene ink exhibits a very low equilibrium contact angle (\sim 0°), expected to be associated with highly divergent evaporation rates at the contact line.^{64,68,69} The graphene ink also forms fingers in the channel corners that are much longer than those formed by both the aqueous PVA system and the PEDOT ink. For example, in 200 μ m wide channels, the graphene ink forms fingers that are nearly 2 mm long, whereas the PEDOT ink and aqueous PVA form fingers that are approximately 700 and 500 μ m long, respectively.

Given the above-described behavior, pinning in the graphene system is expected to be much more pronounced than in the PVA system, and accordingly associated with increased stick-slip behavior and large (\sim 100 μ m/s) velocities at pinning (i.e., critical velocities, v_c). Further, these effects are expected to be more pronounced in wider channels due to the long fingers formed. Yet, the graphene ink defies these expectations and instead exhibits behavior most closely mirroring aqueous PVA when dried at the lowest drying rate, even flowing for *longer* times.

The unique behavior of the graphene ink may be attributable to a resistance to pinning not exhibited by either the aqueous PVA or PEDOT ink systems. As with the PEDOT ink, an increased resistance to pinning can explain the decreased prevalence of stick-slip behavior and low critical pinning velocities. However, the mechanism by which the graphene resists pinning is unaccounted for by reasoning presented thus far. One explanation for how the graphene ink resists pinning is the unique shape of the graphene sheets. Unlike the PVA molecules and PEDOT:PSS particles, which are expected to be near-spherical, the graphene sheets may not pack together or orient themselves effectively at the contact line in such a way that is conducive to contact line pinning. A second reason the graphene ink may resist pinning is due to the stability conferred to it during synthesis. As discussed, the graphene sheets are stabilized using ethyl

cellulose to prevent aggregation.⁷⁷ The same mechanism that stabilizes the graphene sheets in solution may also prevent aggregation at the contact line during capillary flow up until very long times. The low viscosity of the graphene ink (coupled with its weakly shear thinning behavior) is also amenable to long flow distances and times. Indeed, the graphene system is much more complex than the model aqueous PVA system studied in this work, and the exact mode of contact line pinning (or resistance to this pinning) lends itself to further investigation.

The opacity of the black graphene ink precludes measurements of the internal flow field after permanent pinning. However, ref. 77 notes that minimal solids accumulation near the contact line is expected due to Marangoni effects caused by surface tension gradients, which tend to mitigate coffee ring-like effects. Based on this explanation, a recirculating internal flow, similar to that observed in the presence of surfactant, ¹⁰³ is expected after permanent pinning of the graphene ink. This reasoning is consistent with the dry film morphology of the dried graphene film shown in Figure 10d, which indicates a very uniform dry film. It is also possible that these Marangoni effects contribute to the ink's resistance to pinning.

Summary and Conclusions

The influence of drying on the behavior of an aqueous polymer solution in open microchannels was studied. Using aqueous poly(vinyl alcohol) (PVA) as a model system, this influence was investigated over timescales spanning seven orders of magnitude. Key findings, organized by timescale, are summarized below.

Flow down the channel at early times ($t \sim 10^{-3}-10 \text{ s}$) is driven by capillarity and opposed by drying. Analogous to evaporating sessile droplets, this drying is argued to be most pronounced at the contact line where the evaporation rate diverges. The resulting competition between flow and drying leads to impeded contact line motion ('stick-slip' flow) and ultimately to permanent contact line pinning. This is shown to result in strong disagreement between our experimental results with aqueous PVA and predictions based on no drying, especially toward the end of flow ($t \sim 1-10 \text{ s}$). Drying-induced pinning was found to conform to one of three distinct types, each characterized by pinning over a unique timescale and lengthscale. Faster drying rates and intermediate channel widths (50 µm ≤ $W \le 100 \text{ µm}$) were found to be most conducive to

pronounced and repeated pinning events, often leading to a unique 'crawling' motion.

Intermediate times ($t \sim 1-10^2$ s), after the contact line has permanently pinned, are characterized by internal flows which continue to drive polymer to the contact line. These flows are attributed to the uneven evaporative flux over the liquid surface and are reminiscent of the coffee ring effect commonly observed in drying sessile droplets. Pinning to the channel sidewalls is also shown to introduce a weak outward component to this internal flow, away from the center of the channel.

At long times ($t \sim 10-10^3$ s), a drying front forms at the pinned contact line and propagates up the channel toward the reservoir, solidifying the film. The velocity of this drying front is shown to increase as channel width decreases due to drying at the edges of the channel, which becomes significant as channel width decreases. Using confocal Raman microscopy, this drying front was found to be associated with a sharp transition in both film thickness and polymer concentration. The final dry film (the 'capillary coating') is characterized by a significant accumulation of material at the pinned contact line as well as at the walls. Analogies are again drawn between this dry film profile and that seen in dried sessile droplets.

Findings reported in the first part of this article, summarized above, were applied to case studies with PEDOT (poly(3,4-ethylenedioxythiophene)) and graphene inks. These systems are commonly used in the manufacture of printed electronics and possess complexities not present in our model polymer system. While the PEDOT and graphene inks both pin due to drying, both also exhibit significantly less stick-slip behavior compared to that observed in our model polymer system. In the PEDOT ink, this is attributed to gelling of the PEDOT particles in solution as well as its shear thinning rheology. The decreased 'pinnability' of the graphene ink is attributed to the unique shape of the graphene flakes coupled with stabilizers added during its synthesis. Both inks were found to exhibit uniform dry film morphologies with minimal solids accumulation at the contact line.

The findings reported herein can be leveraged to improve the design of capillary coating processes. In general, two key parameters need to be controlled: total flow distance (coating length) and coating uniformity. In this work, we show that total flow distance can be readily modulated by controlling average flow velocity and total flow time. Variables affecting flow velocity in open microchannels are well

understood and viscosity, contact angle, surface tension, and channel width/aspect ratio all constitute "levers" that can be adjusted to tune flow velocity (see eqs. 4–6).

Our results show that total flow time in open microchannels is a complicated function of drying conditions, liquid and channel properties, and flow velocity itself. Here, we show that total flow time can be adjusted by nearly 1000% (see Figure 5a) using only relative humidity. Less intuitive is the significant role that liquid fingers play. For example, large fingers in 200 µm wide channels lead to a significant reduction in total flow time at high drying rates. While alternative channel geometries were not investigated here, our results suggest that channels less-conducive to the formation of liquid fingers (e.g. semi-circular channels) may support longer flow times. At the same time, our results with graphene ink suggest that various additives (e.g. stabilizers) can have a complex and significant influence on total flow time that merits further investigation.

An additional important note is that maximizing flow distance may not always be the ultimate goal. Mahajan et al.¹⁰⁴ demonstrate the utility of being able to precisely control flow distances in complicated, multi-level structures for the manufacture of printed electronic devices. Here, a fundamental understanding of pinning mechanisms can provide invaluable assistance in the precise patterning of capillary coatings within these complicated microstructures. In this work, we have shown that drying rate and subtle changes in a channel's aspect ratio can have a dramatic influence on its pinning behavior (see Supporting Information for additional discussion on this subject).

Coating uniformity is primarily controlled by the evaporative flux profile near the contact line. When the contact line pins mid-way down the channel, the evaporative flux profile achieves maximum nonuniformity, with a significantly increased drying rate near the pinned contact line. The results in Figure 8 show that this dry film uniformity can be enhanced by increasing relative humidity and reducing the overall drying rate. Beyond environmental control, our results with PEDOT and graphene ink (Figures 9d and 10d) suggest that coating chemistry can have a profound influence on dry film uniformity, regardless of the drying rate.

Overall, this work presents a comprehensive study of the capillary coating process, with a detailed

description of how drying influences the behavior of aqueous polymer solutions in open microchannels. The paragraphs above provide examples of the utility of this work and the insight it provides into the understanding and design of the capillary coating process. Direct applications include electronic and catalytic devices which take advantage of the capillary coating process, but this work can also be extended to microfluidic devices employing volatile liquids loaded with solids. While a comparison between our model PVA system and the PEDOT and graphene inks revealed distinct differences, fundamental understandings gained from this work are still able to provide a framework around which to describe the behavior of these complex inks. The specific mechanisms by which these complex inks mitigate stick-slip flow, even at relatively high rates of drying, merit further investigation.

Associated Content

Supporting Information

Details on microchannel fabrication, bulk drying data for all systems and measurement details, rheological behavior of PEDOT and graphene inks, details on confocal Raman microscopy including calibration procedure and raw data, cartoon of type III pinning ('crawling'), detailed discussion of the dependence of pinning behavior on channel width and drying rate, an analysis of the influence of contact line velocity on internal flow to the contact line, and multiple supplemental videos showing pinning and drying in open microchannels. This material is available free of charge via the Internet at http://pubs.acs.org.

Author Information

Corresponding authors

* (L.F.F.) E-mail: lfrancis@umn.edu

Notes

The authors declare no competing financial interests.

Acknowledgements

The authors would like to thank the industrial supporters of the Coating Process Fundamentals Program (CPFP) of the Industrial Partnership for Research in Interfacial and Materials Engineering (IPRIME) for supporting this research. R.K.L.Jr. was further supported by the University of Minnesota Graduate School under the Doctoral Dissertation Fellowship (DDF) program. L.F.F. and K.S.J. gratefully acknowledge support from the National Science Foundation through Grant number CMMI-1634263. K.S.J. further acknowledges support from the National Science Foundation Graduate Research Fellowship Program under Grant No. 00039202. The authors thank Wieslaw Suszynski for high speed video assistance, help designing and constructing the humidity chamber, and for other helpful discussions. The authors would also like to thank Satish Kumar for stimulating discussions, Ethan Secor and Professor Mark Hersam for providing the graphene ink, and Nitika Thakral, whose diligent efforts in the lab during the summer of 2016 inspired some of this work. Lastly, the authors would like to extend their gratitude to colleagues working with printed electronics at the University of Minnesota, including C. Daniel Frisbie, Woo Jin Hyun, Ankit Mahajan, Donghoon Song, Fazel Bidoky, and Motao Cao for providing invaluable feedback throughout this work, especially with respect to its application to printed electronics. Parts of this work were carried out in the Characterization Facility, University of Minnesota, which receives partial support from the NSF through the MRSEC program, and the Minnesota Nano Center, which receives partial support from NSF through the NNCI program.

References

- (1) Schwesinger, N.; Frank, T.; Wurmus, H. A Modular Microfluid System with an Integrated Micromixer. *J. Micromechanics Microengineering* **1996**, *6* (1), 99–102.
- (2) Mainz, M.; Imm, G. An Optimised Split-and-Recombine Micro-Mixer with Uniform 'Chaotic' Mixing. *Lab Chip* **2004**, *4*, 65–69.
- (3) Harrison, D. J.; Fluri, K.; Seiler, K.; Fan, Z.; Effenhauser, C. S.; Manz, A. Micromachining a Miniaturized Capillary Electrophoresis-Based Chemical Analysis System on a Chip. *Science* **1993**, *261*, 895–897.
- (4) Martinez, A. W.; Phillips, S. T.; Whitesides, G. M. Diagnostics for the Developing World: Microfluidic Paper-Based Analytical Devices. *Anal. Chem.* **2010**, *82* (1), 3–10.
- (5) Schoch, R. B.; Han, J.; Renaud, P. Transport Phenomena in Nanofluidics. *Rev. Mod. Phys.* **2008**, *80* (3), 839–883.
- (6) Squires, T. M.; Quake, S. R. Microfluidics: Fluid Physics at the Nanoliter Scale. *Rev. Mod. Phys.* **2005**, 77 (3), 977–1026.
- (7) Di Carlo, D.; Irimia, D.; Tompkins, R. G.; Toner, M. Continuous Inertial Focusing, Ordering, and Separation of Particles in Microchannels. *Proc. Natl. Acad. Sci.* **2007**, *104* (48), 18892–18897.
- (8) Kim, E.; Xia, Y. N.; Whitesides, G. M. Polymer Microstructures Formed by Molding in Capillaries. *Nature*. **1995**, *376*, 581–584.
- (9) Kim, E.; Xia, Y.; Whitesides, G. M. Micromolding in Capillaries: Applications in Materials Science. *J. Am. Chem. Soc.* **1996**, *118*, 5722–5731.
- (10) Shao, F.; Ng, T. W.; Fu, J.; Shen, W.; Ling, W. Y. L. Electrical Circuits from Capillary Flow Driven Evaporation Deposition of Carbon Nanotube Ink in Non-Porous V-Grooves. *J. Colloid Interface Sci.* **2011**, *363* (1), 425–430.
- (11) Mahajan, A.; Hyun, W. J.; Walker, S. B.; Lewis, J. A.; Francis, L. F.; Frisbie, C. D. High-Resolution, High-Aspect Ratio Conductive Wires Embedded in Plastic Substrates. *ACS Appl. Mater. Interfaces* **2015**, *7* (3), 1841–1847.
- (12) Hyun, W. J.; Bidoky, F. Z.; Walker, S. B.; Lewis, J. A.; Francis, L. F.; Frisbie, C. D. Printed, Self-Aligned Side-Gate Organic Transistors with a Sub-5 μm Gate-Channel Distance on Imprinted Plastic Substrates. Adv. Electron. Mater. 2016, 2 (12), 1600293.
- (13) Berthier, J.; Brakke, K. A.; Berthier, E. *Open Microfluidics*; Scrivener Publishing: Beverly, 2016. pp. 13–206, 229–256.
- Ouali, F. F.; McHale, G.; Javed, H.; Trabi, C.; Shirtcliffe, N. J.; Newton, M. I. Wetting Considerations in Capillary Rise and Imbibition in Closed Square Tubes and Open Rectangular Cross-Section Channels. *Microfluid. Nanofluidics* **2013**, *15* (3), 309–326.
- (15) Yang, D.; Krasowska, M.; Priest, C.; Popescu, M. N.; Ralston, J. Dynamics of Capillary-Driven Flow in Open Microchannels. *J. Phys. Chem. C* **2011**, *115*, 18761–18769.
- (16) Sowers, T. W.; Sarkar, R.; Prameela, S. E.; Izadi, E.; Rajagopalan, J. Capillary Driven Flow of Polydimethylsiloxane in Open Rectangular Microchannels. *Soft Matter* **2016**, *12* (12), 5818–5823.

- (17) Chen, T. Capillary Force-Driven Fluid Flow of a Wetting Liquid in Open Grooves with Different Sizes. *Proceedings of the 14th IEEE Intersociety Thermal and Thermomechanical Conference*, Lake Buena Vista, FL, May, 2014; pp. 388–397.
- (18) Ichikawa, N.; Hosokawa, K.; Maeda, R. Interface Motion of Capillary-Driven Flow in Rectangular Microchannel. *J. Colloid Interface Sci.* **2004**, *280* (1), 155–164.
- (19) Khare, K.; Zhou, J.; Yang, S. Tunable Open-Channel Microfluidics on Soft Poly(dimethylsiloxane) (PDMS) Substrates with Sinusoidal Grooves. *Langmuir* **2009**, *25* (21), 12794–12799.
- (20) Rye, R. R.; Yost, F. G.; Mann, J. A. Wetting Kinetics in Surface Capillary Grooves. *Langmuir* **1996**, *12* (96), 4625–4627.
- (21) Mann Jr., J. A.; Romero, L.; Rye, R.; Yost, F. Flow of Simple Liquids Down Narrow V Grooves. *Phys. Rev. E* **1995**, *52* (4), 3967–3972.
- (22) Berthier, J.; Brakke, K. A.; Furlani, E. P.; Karampelas, I. H.; Poher, V.; Gosselin, D.; Cubizolles, M.; Pouteau, P. Whole Blood Spontaneous Capillary Flow in Narrow V-Groove Microchannels. *Sensors Actuators, B Chem.* **2015**, *206*, 258–267.
- (23) Becker, H.; Locascio, L. E. Polymer Microfluidic Devices. *Talanta* **2002**, *56*, 267–287.
- (24) Rye, R. R.; Yost, F. G.; O'Toole, E. J. Capillary Flow in Irregular Surface Grooves. *Langmuir* **1998**, *14* (11), 3937–3943.
- (25) Jokinen, V.; Franssila, S. Capillarity in Microfluidic Channels with Hydrophilic and Hydrophobic Walls. *Microfluid. Nanofluidics* **2008**, *5* (4), 443–448.
- (26) Gong, H.; Beauchamp, M.; Perry, S.; Woolley, A. T.; Nordin, G. P. Optical Approach to Resin Formulation for 3D Printed Microfluidics. *RSC Adv.* **2015**, *5* (129), 106621–106632.
- (27) Lade Jr., R. K.; Hippchen, E. J.; Macosko, C. W.; Francis, L. F. Dynamics of Capillary-Driven Flow in 3D Printed Open Microchannels. *Langmuir* **2017**, *33* (12), 2949–2964.
- (28) Kaigala, G. V; Lovchik, R. D.; Delamarche, E. Microfluidics in the "Open Space" for Performing Localized Chemistry on Biological Interfaces. *Angew. Chem. Int. Ed.* **2012**, *51*, 11224–11240.
- (29) Tian, J.; Kannangara, D.; Li, X.; Shen, W. Capillary Driven Low-Cost V-Groove Microfluidic Device with High Sample Transport Efficiency. *Lab Chip* **2010**, *10* (17), 2258–2264.
- (30) Kachel, S.; Zhou, Y.; Scharfer, P.; Vrančić, C.; Petrich, W.; Schabel, W. Evaporation from Open Microchannel Grooves. *Lab Chip* **2014**, *14* (4), 771–778.
- (31) Werner, G.; Hans-Peter, H. Lancet with Capillary Channel. European Patent 1 911 394 B1, Oct. 14, 2006.
- (32) Calasso, I. G.; Griss, P.; Sarofim, E.; Jaeggi, R.; Kraemer, U.; Hasker, D.; Zimmer, V.; Schmid, W.; Fuerst, O.; List, H.; Haar, H.-P.; Arnitz, T.; Roe, S. N. Body Fluid Sampling Device. U.S. Patent 7,819,822 B2, Oct. 26, 2010.
- (33) Calasso, I. G.; Griss, P.; Sarofim, E.; Jaeggi, R.; Kraemer, U.; Hasker, D.; Zimmer, V.; Schmid, W.; Fuerst, O.; List, H.; Haar, H.-P.; Arnitz, T.; Roe, S. N. Body Fluid Sampling Device. U.S. Patent 8,814,808 B2, Aug. 26, 2014.
- (34) Kumar, M. R.; Dasgupta, S. Modeling of Evaporation from V-Shaped Microgrooves. *Chem. Eng. Commun.* **1997**, *160* (1), 225–248.

- (35) Nilson, R. H.; Griffiths, S. K.; Tchikanda, S. W.; Martinez, M. J. Axially Tapered Microchannels of High Aspect Ratio for Evaporative Cooling Devices. *J. Heat Transfer* **2004**, *126* (3), 453–462.
- (36) Xu, X.; Carey, V. P. Film Evaporation from a Micro-Grooved Surface An Approximate Heat Transfer Model and Its Comparison with Experimental Data. *J. Thermophys. Heat Transf.* **1989**, *4* (4), 512–520.
- (37) Bai, L.; Lin, G.; Peterson, G. P. Evaporative Heat Transfer Analysis of a Heat Pipe With Hybrid Axial Groove. *J. Heat Transfer* **2013**, *135* (3), 31503.
- (38) Nilson, R. H.; Tchikanda, S. W.; Griffiths, S. K.; Martinez, M. J. Steady Evaporating Flow in Rectangular Microchannels. *Int. J. Heat Mass Transf.* **2006**, *49* (9–10), 1603–1618.
- (39) Peela, N. R.; Mubayi, A.; Kunzru, D. Washcoating of γ-Alumina on Stainless Steel Microchannels. *Catal. Today* **2009**, *147S*, S17–S23.
- (40) Hyun, W. J.; Secor, E. B.; Kim, C.-H.; Hersam, M. C.; Francis, L. F.; Frisbie, C. D. Scalable, Self-Aligned Printing of Flexible Graphene Micro-Supercapacitors. *Adv. Energy Mater.* **2017**, *7* (17), 1700285.
- (41) Lone, S.; Zhang, J. M.; Vakarelski, I. U.; Li, E. Q.; Thoroddsen, S. T. Evaporative Lithography in Open Microfluidic Channel Networks. *Langmuir* **2017**, *33* (11), 2861–2871.
- (42) Baret, J. C.; Decré, M. M. J.; Herminghaus, S.; Seemann, R. Transport Dynamics in Open Microfluidic Grooves. *Langmuir* **2007**, *23* (17), 5200–5204.
- (43) Berthier, J.; Brakke, K. A.; Gosselin, D.; Huet, M.; Berthier, E. Metastable Capillary Filaments in Rectangular Cross-Section Open Microchannels. *AIMS Biophys.* **2014**, *1* (1), 31–48.
- (44) Romero, L. A.; Yost, F. G. Flow in an Open Channel Capillary. J. Fluid Mech. 1996, 322, 109–129.
- (45) Quéré, D. Inertial Capillarity. Europhys. Lett. 1997, 39 (5), 533-538.
- (46) Stange, M.; Dreyer, M. E.; Rath, H. J. Capillary Driven Flow in Circular Cylindrical Tubes. *Phys. Fluids* **2003**, *15* (9), 2587–2601.
- (47) Popescu, M. N.; Ralston, J.; Sedev, R. Capillary Rise with Velocity-Dependent Dynamic Contact Angle. *Langmuir* **2008**, *24* (21), 12710–12716.
- (48) Fries, N.; Dreyer, M. The Transition from Inertial to Viscous Flow in Capillary Rise. *J. Colloid Interface Sci.* **2008**, 327 (1), 125–128.
- (49) Bosanquet, C. H. On the Flow of Liquids into Capillary Tubes. *Philos. Mag. J. Sci.* **1923**, *6*, 525–531.
- (50) Lucas, R. Rate of Capillary Ascension in Liquids. *Colloid Polym. Sci.* **1918**, *23*, 15–22.
- (51) Washburn, E. W. The Dynamics of Capillary Flow. *Phys. Rev.* **1921**, *17* (3), 273–283.
- (52) Rideal, E. K. On the Flow of Liquids under Capillary Pressure. *Philos. Mag. Ser.* **1922**, *44*, 1152–1159.
- (53) Girardo, S.; Palpacelli, S.; De Maio, A.; Cingolani, R.; Succi, S.; Pisignano, D. Interplay between Shape and Roughness in Early-Stage Microcapillary Imbibition. *Langmuir* **2012**, *28* (5), 2596–2603.
- (54) Siebold, A.; Nardin, M.; Schultz, J. Effect of Dynamic Contact Angle on Capillary Rise Phenomena. *Colloids Surfaces A* **2000**, *161* (1), 81–87.

- (55) Chebbi, R. Dynamics of Liquid Penetration into Capillary Tubes. *J. Colloid Interface Sci.* **2007**, *315* (1), 255–260.
- (56) Hamraoui, A.; Thuresson, K.; Nylander, T.; Yaminsky, V. Can a Dynamic Contact Angle Be Understood in Terms of a Friction Coefficient? *J. Colloid Interface Sci.* **2000**, *226* (2), 199–204.
- (57) Hamraoui, A.; Nylander, T. Analytical Approach for the Lucas-Washburn Equation. *J. Colloid Interface Sci.* **2002**, *250* (2), 415–421.
- (58) Blake, T. D.; De Coninck, J. The Influence of Pore Wettability on the Dynamics of Imbibition and Drainage. *Colloids Surfaces A* **2004**, *250*, 395–402.
- (59) Szekely, J.; Neumann, A. W.; Chuang, Y. K. The Rate of Capillary Penetration and the Applicability of the Washburn Equation. *J. Colloid Interface Sci.* **1971**, *35* (2), 273–278.
- (60) Levine, S.; Reed, P.; Watson, E. J.; Neale, G. A Theory of the Rate of Rise of a Liquid in a Capillary. In *Colloid and Interface Science*; Kerker, M., Ed.; Academic Press Inc.: New York, 1976; Vol. III; pp 403–419.
- (61) Levine, S.; Lowndes, J.; Watson, E.; Neale, G. A Theory of Capillary Rise of a Liquid in a Vertical Cylindrical Tube and in a Paralle-Plate Channel. *J. Colloid Interface Sci.* **1980**, *73* (1), 136.
- (62) Martic, G.; Gentner, F.; Seveno, D.; Coulon, D.; De Coninck, J.; Blake, T. D. A Molecular Dynamics Simulation of Capillary Imbibition. *Langmuir* **2002**, *18* (21), 7971–7976.
- (63) Chen, Y.; Melvin, L. S.; Rodriguez, S.; Bell, D.; Weislogel, M. M. Capillary Driven Flow in Micro Scale Surface Structures. *Microelectron. Eng.* **2009**, *86* (4–6), 1317–1320.
- (64) Hu, H.; Larson, R. G. Evaporation of a Sessile Droplet on a Substrate. *J. Phys. Chem. B* **2002**, *106* (6), 1334–1344.
- (65) Wang, H.; Murthy, J. Y.; Garimella, S. V. Transport from a Volatile Meniscus inside an Open Microtube. *Int. J. Heat Mass Transf.* **2008**, *51* (11–12), 3007–3017.
- (66) Rio, E.; Daerr, A.; Lequeux, F.; Limat, L. Moving Contact Lines of a Colloidal Suspension in the Presence of Drying. *Langmuir* **2006**, *22* (7), 3186–3191.
- (67) Monteux, C.; Elmaallem, Y.; Narita, T.; Lequeux, F. Advancing-Drying Droplets of Polymer Solutions: Local Increase of the Viscosity at the Contact Line. *Europhys. Lett.* **2008**, *83* (3), 34005.
- (68) Deegan, R. D.; Bakajin, O.; Dupont, T. F.; Huber, G.; Nagel, S. R.; Witten, T. A. Capillary Flow as the Cause of Ring Stains from Dried Liquid Drops. *Nature* **1997**, *389* (6653), 827–829.
- (69) Deegan, R. D. Contact Line Deposits in an Evaporating Drop. *Phys. Rev.* **2000**, *62* (1), 756.
- (70) Berteloot, G.; Pham, C.-T.; Daerr, A.; Lequeux, F.; Limat, L. Evaporation-Induced Flow near a Contact Line: Consequences on Coating and Contact Angle. *Europhys. Lett.* **2008**, *83* (1), 14003.
- (71) Shikhmurzaev, Y. D. Moving Contact Lines: An Overview. In *Capillary Flows with Forming Interfaces*; Chapman & Hall/CRC Press: Boca Raton, 2007; pp 108–113.
- (72) Dussan, E. B.; Davis, S. H. On the Motion of a Fluid-Fluid Interface along a Solid Surface. *J. Fluid Mech.* **1974**, *65* (1), 71–95.
- (73) Weon, B. M.; Je, J. H. Self-Pinning by Colloids Confined at a Contact Line. *Phys. Rev. Lett.* **2013**, 110 (2), 1–5.

- (74) Sangani, A. S.; Lu, C.; Su, K.; Schwarz, J. A. Capillary Force on Particles near a Drop Edge Resting on a Substrate and a Criterion for Contact Line Pinning. *Phys. Rev. E* **2009**, *80* (1), 11603.
- (75) Pritchard, J. *Poly (Vinyl Alcohol): Basic Properties and Uses*; Gordon and Breach Science Publishers: London, 1970. pp 60–63, 65–80
- (76) Graphene ink provided by Ethan Secor and Professor Mark Hersam of Northwestern University.
- (77) Secor, E. B.; Prabhumirashi, P. L.; Puntambekar, K.; Geier, M. L.; Hersam, M. C. Inkjet Printing of High Conductivity, Flexible Graphene Patterns. *J. Phys. Chem. Lett.* **2013**, *4* (8), 1347–1351.
- (78) Lade, R. K.; Song, J.-O.; Musliner, A. D.; Williams, B. A.; Kumar, S.; Macosko, C. W.; Francis, L. F. Sag in Drying Coatings: Prediction and Real Time Measurement with Particle Tracking. *Prog. sOrg. Coatings* **2015**, *86*, 49–58.
- (79) Lade Jr., R. K. Flow and Drying Dynamics in Gravity- and Capillary-Driven Coating Processes. PhD Dissertation, University of Minnesota, Minneapolis, MN, 2017.
- (80) Ludwig, I.; Schabel, W.; Kind, M. Drying and Film Formation of Industrial Waterborne Latices. *AIChE J.* **2007**, *53* (3), 549–560.
- (81) Nasarek, R.; Wereley, S.; Stephan, P. Flow Field Measurements near a Moving Meniscus of a Capillary Flow with Micro Particle Image Velocimetry (μPIV). *Proceedings of the 6th International Conference on Nanochannels, Microchannels, Minichannels*, Darmstadt, Germany, June, 2008. pp 863–871.
- (82) Queralt-Martín, M.; Pradas, M.; Rodríguez-Trujillo, R.; Arundell, M.; Corvera Poiré, E.; Hernández-Machado, A. Pinning and Avalanches in Hydrophobic Microchannels. *Phys. Rev. Lett.* **2011**, *106* (19), 194501.
- (83) Kusumaatmaja, H.; Pooley, C. M.; Girardo, S.; Pisignano, D.; Yeomans, J. M. Capillary Filling in Patterned Channels. *Phys. Rev. E* **2008**, 77 (2), 3–6.
- (84) Mognetti, B. M.; Yeomans, J. M. Capillary Filling in Microchannels Patterned by Posts. *Phys. Rev. E* **2009**, *80* (5), 56309.
- (85) Blake, T. D. Dynamic Contact Angles and Wetting Kinetics. In *Wettability*; Berg, J. C., Ed.; Marcel Dekker, Inc.: New York, 1993; pp 251–273.
- (86) Adam, N. K. Principles of Penetration of Liquids into Solids. *Discuss. Faraday Soc.* **1948**, *3*, 5–11.
- (87) Shuttleworth, R.; Bailey, G. L. J. The Spreading of a Liquid over a Rough Solid. *Discuss. Faraday Soc.* **1948**, *3* (16), 16.
- (88) Dettre, R. H.; Johnson, R. E. Contact Angle Hysteresis. I. Study of an Idealized Rough Surface. In *Contact Angle, Wettability, and Adhesion*; Fowkes, F. M., Ed.; American Chemical Society: Washington, D. C., 1964; Vol. 43, pp 112–135.
- (89) Huh, C.; Mason, S. G. Effects of Surface Roughness on Wetting (Theoretical). *J. Colloid Interface Sci.* **1977**, *60* (1), 11–38.
- (90) Concus, P.; Finn, R. On the Behaviour of a Capillary Surface in a Wedge. *Proc. Natl. Acad. Sci. U. S. A.* **1969**, *63* (2), 292–299.
- (91) Weislogel, M. M.; Lichter, S. Capillary Flow in an Interior Corner. *J. Fluid Mech.* **1998**, *373*, 349–378.

- (92) Seemann, R.; Brinkmann, M.; Kramer, E. J.; Lange, F. F.; Lipowsky, R. Wetting Morphologies at Microstructured Surfaces. *Proc. Natl. Acad. Sci.* **2005**, *102* (6), 1848–1852.
- (93) Walker, S. B.; Lewis, J. A. Reactive Silver Inks for Patterning High-Conductivity Features at Mild Temperatures. *J. Am. Chem. Soc.* **2012**, *134* (3), 1419–1421.
- (94) Jung, Y.; Kajiya, T.; Yamaue, T.; Doi, M. Film Formation Kinetics in the Drying Process of Polymer Solution Enclosed by Bank. *Jpn. J. Appl. Phys.* **2009**, *48* (3), 31502.
- (95) Price, K. K.; McCormick, A. V.; Francis, L. F. CryoSEM Investigation of Latex Coatings Dried in Walled Substrates. *Langmuir* **2012**, *28*, 10329–10333.
- (96) Popov, Y. O. Evaporative Deposition Patterns: Spatial Dimensions of the Deposit. *Phys. Rev. E* **2005**, 7*I* (3), 36313.
- (97) Leng, J. Drying of a Colloidal Suspension in Confined Geometry. *Phys. Rev. E* **2010**, *82* (2), 21405.
- (98) Routh, A. F.; Russel, W. B. Horizontal Drying Fronts during Solvent Evaporation from Latex Films. *AIChE J.* **1998**, *44* (9), 2088–2098.
- (99) Zhang, S.; Yu, Z.; Li, P.; Li, B.; Isikgor, F. H.; Du, D.; Sun, K.; Xia, Y.; Ouyang, J. Poly(3,4-Ethylenedioxythiophene):polystyrene Sulfonate Films with Low Conductivity and Low Acidity through a Treatment of Their Solutions with Probe Ultrasonication and Their Application as Hole Transport Layer in Polymer Solar Cells and Perovskite Solar Cells. *Org. Electron.* **2016**, *32*, 149–156.
- (100) Nagy, D. J. Size Exclusion Chromatography of Polyvinyl Alcohol and Polyvinyl Acetate. In *Handbook of Size Exclusion Chromatography and Related Techniques*; Wu, C.-S., Ed.; Marcel Dekker, Inc.: New York, 2004; pp 279–281.
- (101) Digilov, R. M. Capillary Rise of a Non-Newtonian Power Law Liquid: Impact of the Fluid Rheology and Dynamic Contact Angle. *Langmuir* **2008**, *24* (23), 13663–13667.
- (102) Xing, R.; Wang, S.; Zhang, B.; Yu, X.; Ding, J.; Wang, L.; Han, Y. Inkjet Printed Polystyrene Sulfuric Acid-Doped poly(3,4-Ethylenedioxythiophene) (PEDOT) Uniform Thickness Films in Confined Grooves through Decreasing the Surface Tension of PEDOT Inks. *RSC Adv.* **2017**, *7* (13), 7725–7733.
- (103) Still, T.; Yunker, P. J.; Yodh, A. G. Surfactant-Induced Marangoni Eddies Alter the Coffee-Rings of Evaporating Colloidal Drops. *Langmuir* **2012**, *28* (11), 4984–4988.
- (104) Mahajan, A.; Hyun, W. J.; Walker, S. B.; Rojas, G. A.; Choi, J.; Lewis, J. A.; Francis, L. F.; Frisbie, C. D. A Self-Aligned Strategy for Printed Electronics: Exploiting Capillary Flow on Microstructured Plastic Surfaces. *Adv. Electron. Mater.* **2015**, *I* (9), 1500137.

Table of Contents graphic

